# Inferences from Surface Thermal Emission of Young Neutron Stars

Jason Alan Jackson Alford

Submitted in partial fulfillment of the
requirements for the degree
of Doctor of Philosophy
in the Graduate School of Arts and Sciences

COLUMBIA UNIVERSITY

2020

# ABSTRACT

## Inferences from Surface Thermal Emission of Young Neutron Stars

Jason A. J. Alford

We consider the question of the magnetic field configuration of central compact objects (CCOs), specifically if their observed spectra allow uniform surface temperatures and carbon atmospheres. Although it is theoretically plausible that young hot neutron stars will deplete their hydrogen and helium atmospheres through diffusive nuclear burning, we find that there is no strong observational evidence to suggest that any particular CCO has a uniform temperature carbon atmosphere. In fact, they all may have small hot spots, similar to what we have measured on the surface of RX J0822 4300, and what has been observed in the cases of two other CCOs, 1E 1207.4 5209 and PSR J1852+0040. We find it is likely that most CCOs have small magnetic inclination angles.

We also study the magnetic field configurations of two particular young neutron stars through general relativistic modeling of the X-ray light curves produced by their thermal surface emission. In particular, we have analyzed over a decade of *XMM-Newton* observations of the central compact object RX J0822 4300 and also the transient magnetar XTE J1810 197. We show that the CCO RX J0822 4300 has two heated regions with very different sizes and temperatures, and we measure a significant deviation angle from a purely antipodal geometry. This measurement can inform theoretical models of the strength and geometry of the crustal magnetic fields that conduct heat to toward these hot spots. We measure the size, temperature, angular emission pattern and viewing geometry toward the

heated surface regions of the magnetar XTE J1810  197 in the years following its 2003 outburst. We demonstrate that, after the size and the temperature of the heated region shrank from what was measured in the initial outburst, the magnetar eventually entered a steady state with the hot spot luminosity powered by magnetic field decay. We find that the magnitude of the flux from the whole surface of XTE J1810  197, combined with several distance estimates, indicates that the mass of XTE J1810  197 must be significantly larger than the canonical 1.4 M  neutron star.

# Contents

# List of Figures

# List of Tables

# Acknowledgements

Firstly, I thank my parents, whose love and encouragement helped me to make it this far. I thank my wife Ayelet, who has helped me through through my PhD work from the very beginning. Our relationship has given me much needed love, balance and perspective.

I would like to thank Eric Gotthelf for his generous advice on data analysis, statistical issues and much more. I am also grateful to Rosalba Perna for sharing her helpful insights and encouragement.

Finally, I would like to express my gratitude towards my great thesis advisor Jules Halpern. His advice and kindness have supported me immensely as I navigated the challenges of research. I am very fortunate to have had his guidance and support.

2020, New York, NY

# Chapter 1

# Introduction

## 1.1 Early Neutron Star Predictions and Observations

Neutron stars (NSs) were predicted several decades prior to the radio observations that confirmed their existence. There is actually some difficulty pinpointing who was first to predict the existence of neutron stars. In a brief 1932 paper Lev Landau wrote about stars that he expected to form "when the density of matter becomes so great that atomic nuclei come in close contact, forming one gigantic nucleus" (Landau 1932). Landau apparently believed that all stars more massive than the Chandrasekhar limit would look like giant nuclei (he didn't anticipate the existence of massive non-degenerate stars), which at that time he believed consisted of just electrons and protons, since the neutron had not yet been discovered. See Yakovlev et al. (2013) for an interesting discussion of Landau's prediction in its historical context.

Baade & Zwicky (1934) made the first detailed prediction of the existence of neutron stars, with the benefit of the discovery of the neutron by Chadwick in 1932. They wrote "With all reserve we advance the view that a super-nova represents the transition of an

ordinary star into a neutron star, consisting mainly of neutrons. Such as star may possess a very small radius and an extremely high density."

Radio emission from pulsars was first discovered in 1967 when Jocelyn Bell observed regular 1.337 s pulsations from the object that we now know as PSR B1919+21 (Hewish et al. 1968). In this discovery paper, they did speculate that a neutron star could be origin of the radio emission, but did not understand that rotation must be the cause of the very precise periodicity. Soon after the radio discovery, Gold (1968) proposed that a rapidly rotating neutron star must be the origin of the regular radio pulsations.

## 1.2 Physical Parameters of Neutron Stars

Neutron stars can be divided into several classes by measuring their rotation periods $P$ and their rotation period derivatives $\dot{P}$, and plotting them in a diagram as shown in Figure 1.1. This type of figure is particularly useful because there are three important physical quantities than can be estimated by measuring just these two physical parameters. These three quantities are the neutron star dipole magnetic field strength, the maximum age of the NS, and the rate of rotational energy loss. If we assume that the primary braking mechanism is magnetic dipole radiation, as one expects to be the case for the isolated neutron stars in this diagram which shouldn't have significant external torques from accretion, etc., the surface dipole magnetic field strength is given by:

$$B_s \quad 3.2 \quad 10^{19}\sqrt{P\dot{P}}\ \mathrm{G} \tag{1.1}$$

If a neutron star is steadily spinning down and its current period is significantly greater than its period at birth, then its true age is well approximated by its characteristic age $\tau_c$:

$$\tau_c = \frac{P}{2\dot{P}} \tag{1.2}$$

We can also estimate the rate of rotational energy loss $\dot{E}$ by approximating the neutron star moment of inertia as $I = 10^{45}$ g cm$^2$:

$$\dot{E} = 3.95 \quad 10^{46}\dot{P}\left(\frac{P}{s}\right)^{3} I_{45} \text{ erg/s} \tag{1.3}$$

In the upper right of Figure 1.1 we find the magnetars, which stand out due to their strong ( $10^{14}$ G) magnetic fields and young spin-down ages. A major subject of this thesis, XTE J1810 197, is indicated in the figure. Magnetars are believed to be young neutron stars because of their 1 100 kyr characteristic ages and the association of some magnetars with young supernova remnants.

Toward the middle of the diagram we have the three central compact objects (CCOs) with measured periods and period derivatives. These three CCOs are RX J0822 4300, PSR J1852+0040, and 1E 1207.4 5209. RX J0822 4300, in the Puppis A supernova remnant, is the subject of Chapter 3 and is indicated in the figure. CCOs have characteristic ages that are much larger than their associated young supernova remnants because they have relatively small $\dot{P}$ values, and therefore their current spin periods are close to the birth values.

Determining the maximum mass of a neutron star would place strong constraints on the allowed NS equations of state, which in turn would place interesting constraints on the equation of state of cold dense nuclear matter. Early on, Oppenheimer & Volkoff (1939) calculated a maximum mass of 0.7M with a simple model that ignored strong nuclear forces. While it is now known that the NS mass limit is much greater than this, the limit is known as the Tolman-Oppenheimer-Volkoff (TOV) limit, after the authors of this paper and earlier work by Tolman.

Margalit & Metzger (2017) combined data from the LIGO detection of the gravitational wave GW170817 with electromagnetic follow-up observations to derive an upper limit on the maximum mass of a neutron star, $M_{\mathsf{max}}$ . 2.17 M . Empirically, we know of the existence of several very massive neutron stars such as PSR J1614 2230 and PSR J0348+0432 with masses of 1.97 0.04 M and 2.01 0.04 M , respectively (Demorest et al. 2010; Antoniadis et al. 2013). Even more recently, Linares et al. (2018) measured the mass of a redback pulsar to be $2.27^{+0.17}_{0.15}$ M , and Cromartie et al. (2019) measured the mass of the millisecond pulsar PSR J0740+6620 to be $2.17^{+0.11}_{0.10}$ M . In this thesis, we will present evidence that XTE J1810 197 may be among these most massive neutron stars.

## 1.3 X-ray Observations of Magnetars and CCOs

This section will review the observations that led to the establishment of magnetars and CCOs as two (of several) classes of neutron stars. This will provide important context for the modeling of the transient magnetar XTE J1810 197 presented in Chapter 4 and the modeling of the central compact object RX J0822 4300 presented in Chapter 3.

### 1.3.1 Establishing Magnetars as a Class of Neutron Stars

The first magnetar detection was a gamma-ray burst from a source located in the Large Magellanic Cloud that is now known as SGR 0526 66 (Mazets et al. 1979). Subsequent observations of objects similar to SGR 0526 66 led to the designation of such phenomena as Soft Gamma-ray Repeaters (SGRs). In 1980 the first Anomalous X-ray Pulsar (AXP) was observed with 3.489 s pulse period (Gregory & Fahlman 1980; Fahlman & Gregory 1981). AXPs were initially named after the accretion-powered X-ray pulsars, because their luminosities were too high to be rotation powered, and it was not yet understood that the

power source is magnetic energy.

After over a decade of observations, Duncan & Thompson (1992) proposed the magnetar model where high energy bursts are produced by neutron stars with magnetic fields that are two to three orders of magnitude greater than the $10^{12}$ G magnetic fields typical of isolated radio pulsars. Subsequently Thompson & Duncan (1996) suggested that SGRs and AXPs are both manifestations of magnetars and that AXPs should also display SGR-like bursting behavior and glitches. SGR 1806 20 was the first magnetar with a measured spin-down rate, indicating a dipole magnetic field strength of 8 $10^{14}$ G and providing strong observational support for the magnetar model (Kouveliotou et al. 1998).

It is now understood that magnetars can be divided into two groups often termed the 'persistent' magnetars and the 'transient' magnetars. About half of all magnetars are in the transient category, i.e. they have 'quiescent' luminosities of about $10^{32}$ erg s $^{1}$ or less. During their outbursts transient magnetars reach luminosities of $10^{35}$ erg s $^{1}$, comparable to the steady state of the persistent magnetars. The underlying physical mechanism that distinguishes transient magnetars from persistent magnetars is an interesting open question.

Transient magnetars were not discovered until the 2003 outburst of XTE J1810 197 (Ibrahim et al. 2004). In addition to revealing the existence of this new class of magnetars, XTE J1810 197 was also the first magnetar observed to be a source of radio emission (Halpern et al. 2005; Camilo et al. 2006). The spectrum of XTE J1810 197 was well described by a 0.7 keV and 0.3 keV two blackbody model, and the temperatures of these two blackbodies were observed to decrease in the years following the outburst (Gotthelf & Halpern 2007). This data is consistent with the untwisting magnetosphere model of Beloborodov (2009), which predicts shrinking and cooling hot spots on the surface of magnetars. In this theory the outburst is triggered by the crustal failure which twists the strong magnetic field anchored to the crust of the magnetar. With continuing X-ray observations, it was later

evident that there is also a softer 0.15 keV blackbody component in the spectrum of XTE J1810 197 with an area so large that must correspond to emission from the entire NS surface (Bernardini et al. 2009). Alford & Halpern (2016) analyzed over ten years of observations and fit the spectrum of XTE J1810 197 with a 'three-to-two blackbody'model. In this model the spectrum is well fit with a three blackbody model at earlier times and a two blackbody model at later times, with the whole surface component present at all epochs. Alford & Halpern (2016) found that XTE J1810 197 entered a steady state about six years post outburst, and that in this steady state there is still a 0.3 keV hot spot with a luminosity that exceeds the spin-down power. This indicated that this transient magnetar was still magnetically powered even many years post-outburst. Alford & Halpern (2016) used simple blackbody models and did not use a general relativistic model to accurately measure the size of the heated regions and the viewing geometry as a function of time post-outburst, which is the subject of Chapter 4 of this thesis.

There are now about a dozen known transient magnetars. Four of them have been detected as radio emitters and many of them have shrinking and cooling hot spots, similar to what was originally observed in the case of XTE J1810 197.

### 1.3.2 Establishing Central Compact Objects as a Class of Neutron Stars

Pavlov et al. (2000) coined the term 'central compact object' when referring to the radio quiet X-ray point source with a thermal spectrum in the Cas A supernova remnant. It was unclear then what physical connection might exist to unite the few similar object in supernova remnants. The nature of CCOs has become more clear recently with efforts to measure the periods and period derivatives of CCOs through X-ray timing studies. However, at this present time, no X-ray pulsations have been detected from the CCO in Cas A, as

well as from four of the other eight confirmed CCOs.

The first measured CCO spin period was report by Zavlin et al. (2000), who measured 0.424 s X-ray pulsations from 1E 1207.4  5209. Then, in 2005, pulsations from PSR J1852+0040 with a 0.105 s period were reported by Gotthelf et al. (2005). The spin-down rate of PSR J1852+0040, the first such measurement for a CCO, was reported by Halpern & Gotthelf (2010), and implied a small 3.1  $10^{10}$ G dipole field strength. Suspecting that these weak dipole magnetic fields and slow spin periods at birth are a physical basis of the CCO class, they named these objects 'anti-magnetars'. In 2013, Gotthelf et al. (2013) reported measurements of the spin-down rates of RX J0822  4300 and 1E 1207.4  5209 and found that they also implied small dipole magnetic field strengths of 2.9  $10^{10}$ G and 9.8  $10^{10}$ G, respectively. Interestingly the spin-down powers of these three CCOs are much smaller than their X-ray luminosities, indicating that the energy source is likely residual heat from their recent births. The hot spots observed on CCOs can be accounted for by this residual heat being conducted anisotropically within the NS crust. See De Luca (2017) for a short review of CCOs.

## 1.4 General Relativistic Modeling of the X-ray Light Curves Produced by Hot Spots on Neutron Stars

Neutron stars are relativistic objects and the interpretation of their emission must include effects that become important in strong gravitational fields. For relatively slowly rotating neutron stars such magnetars and CCOs, all of which have spin periods $P > 0.1$ s, there are two relativistic effects to include in the model. First, there is gravitational redshift effect where the energy of a detected photon is lower than the energy of the photon emitted in the rest frame of the star. Second, due to light bending, more than half of the surface area is

visible to an observer 'at infinity'. Emission models of neutron stars with faster spin periods must include beaming and the kinematic Doppler-shift.

Due to the gravitational redshift, for each photon with energy $E$ emitted at the surface of a neutron star with radius $R$ , an observer will record a photon with energy $E_1$ according to the relation:

$$E_1 = \sqrt{1 \quad \frac{r_g}{R}}\, E \tag{1.4}$$

$$r_g = \frac{2GM}{c^2} \tag{1.5}$$

In this thesis we will be modeling the energy-dependent pulse profiles of neutron stars by calculating the flux from hot spots as the hot spot position (relative to the observer) changes with rotation of the star. To do this we consider the flux from an infinitesimal region on the NS surface. A photon initially emitted at an angle $\delta$ with respect to the radial direction will reach a distant observer who measures the colatitude of the emission point to be $\theta$. See Figure 1.2 for a diagram of these angles and an example photon trajectory. In flat spacetime the emission angle and colatitude are equal. In a Schwarzschild geometry the colatitude $\theta$ as a function of the emission angle $\delta$ is given by the following elliptic integral derived in Pechenick et al. (1983):

$$\theta(\delta) = \int_0^{r_g/2R} x\, du \Big/ \sqrt{\left(1 \quad \frac{r_g}{R}\right)\left(\frac{r_g}{2R}\right)^2 \quad (1 \quad 2u)u^2x^2} \tag{1.6}$$

$$x \quad \sin(\delta) \tag{1.7}$$

For simplicity, we use an approximate relationship between photon emission angle $\delta$ and

the colatitude $\theta$ derived by Beloborodov (2002),

$$1 \quad \cos(\delta) = (1 \quad \cos(\theta)) \left(1 \quad \frac{r_g}{R}\right). \tag{1.8}$$

This relationship is more accurate for smaller $\delta$ and $r_g/R$. Figure 2 in Beloborodov (2002) shows the numerical accuracy as a function of $\delta$ and $r_g/R$. For a typical 1.4 M neutron star with a 12 km radius $r_g/R = 0.344$, and the relationship is accurate to better than 1% for $\delta < 80$ degrees, and is accurate to better than 2% for $\delta > 80$ degrees.

The flux $dF$ a distant observer measures from a small area $dS$ on the neutron star surface is:

$$dF = \left(1 \quad \frac{r_g}{R}\right) I_0(\delta)\cos(\delta)\frac{d\cos(\delta)}{d\cos(\theta)}\frac{dS}{D^2} \tag{1.9}$$

This is equation A3 derived in the appendix of Beloborodov (2002). $I_0(\delta)$ is the radiation intensity in the NS frame, and $D$ is the distance to the NS. Inserting equation 1.8 for $\frac{d\cos(\delta)}{d\cos(\theta)}$ we get equation 4 from Beloborodov (2002).

$$dF = \left(1 \quad \frac{r_g}{R}\right)^2 I_0(\delta)\cos(\delta)\frac{dS}{D^2} \tag{1.10}$$

We use this equation to calculate the sizes of the heated NS surface regions and also to calculate the pulse profiles. To speed up these calculations, we separate out the integration of $dF$ into two parts, the integration of cos $(\delta)$ and the integration of the surface element $dS$. We only integrate over the surface area of the hot region, unlike previous techniques which integrate over the entire neutron star surface. We consider simple spherical caps, with area $2\pi(1 \quad \cos(r))$, where r is the angular radius of the spherical cap. In the case where the hot spot partially intersects the invisible region of the NS surface, we calculate the area of the intersection region and subtract it from the spherical cap area. The area of the intersection

region $I(\theta, r_1, r_2)$ is given below, where $\theta$ is the angular distance from the center of the hot spot to the center of the invisible region, $r_1$ is the angular radius of the hot spot and $r_2$ is the angular radius of the invisible region:

$$I(\theta, r1, r2) = 2\pi \quad 2\cos^{-1}\left(\frac{\cos(\theta)}{\sin(r_1)\sin(r_2)} \quad \frac{1}{\tan(r_1)\tan(r_2)}\right)$$

$$2\cos^{-1}\left(\frac{\cos(r_2)}{\sin(\theta)\sin(r_1)} \quad \frac{1}{\tan(\theta)\tan(r_1)}\right)\cos(r_1) \quad 2\cos^{-1}\left(\frac{\cos(r_1)}{\sin(\theta)\sin(r_2)} \quad \frac{1}{\tan(\theta)\tan(r_2)}\right)\cos(r_2) \tag{1.11}$$

Now the calculation of the area of the hot spot is just a trigonometric calculation instead of a two dimensional integration. Furthermore, symmetry can be used to make integration of $\cos(\delta)$ into a one dimensional integral inside the hot spot. For large hot spots (i.e. angular radii $> 10$ degrees) we can calculate fluxes more accurately with just $10^2$ integration elements versus $10^5$ integration elements over the whole neutron star surface. For smaller hot spots, integration may be unnecessary and a simple point approximation may be used instead. This integration technique is most useful for magnetars which often do have very large emitting regions.

## 1.5 Outline of Thesis

Chapter 2 will present X-ray observations of all eight confirmed CCOs, and some candidate CCOs, with the goal of understanding what constraints may be placed on their atmospheric composition and surface temperature geometry. I will attempt to fit all of their spectra with single temperature carbon atmosphere models, with reasonable values for the distance and

NS radius. I will determine how 'easy' it is to fit this carbon atmosphere model to all CCOs, even the three CCOs that are known to not have single-temperature carbon atmospheres. I will show that is plausible that most of the CCOs that can be successfully described by a single-temperature carbon atmosphere are actually cousins of RX J0822 4300, 1E 1207.4 5209, and PSR J1852+0040, with hot spots that cover only a small fraction of the NS surface. Lastly, I will make some inferences about the distribution of CCO magnetic inclination angles, which may point toward a better understanding of the physics of this class of young neutron stars.

Chapter 3 will present detailed X-ray modeling of the energy-dependent pulse profile of RX J0822 4300, the CCO in the Puppis A SNR, and measure the size of the deviation from a pure axial-symmetric geometry. I will discuss the implications for the subsurface magnetic field geometry.

In Chapter 4 I will present X-ray observations and modelling of the transient magnetar XTE J1810 197. I will measure the size, temperature and luminosity of its heated surface region during its post-outburst steady state. Constraints on the viewing geometry of this magnetar will be calculated. I will show that the emission from the whole of surface of the NS is sufficient to produce its post-outburst, steady state energy-dependent pulse profiles, without the need to invoke anisotropic emission as had been previously assumed. I will suggest that this detailed X-ray pulsed profile modeling, combined with independent distance estimates for XTE J1810 197, is the first observational evidence that magnetars are significantly more massive than the canonical 1.4 solar mass neutron star.

Finally, in Chapter 5, I will summarize the key results of this thesis and describe several interesting directions for future work.

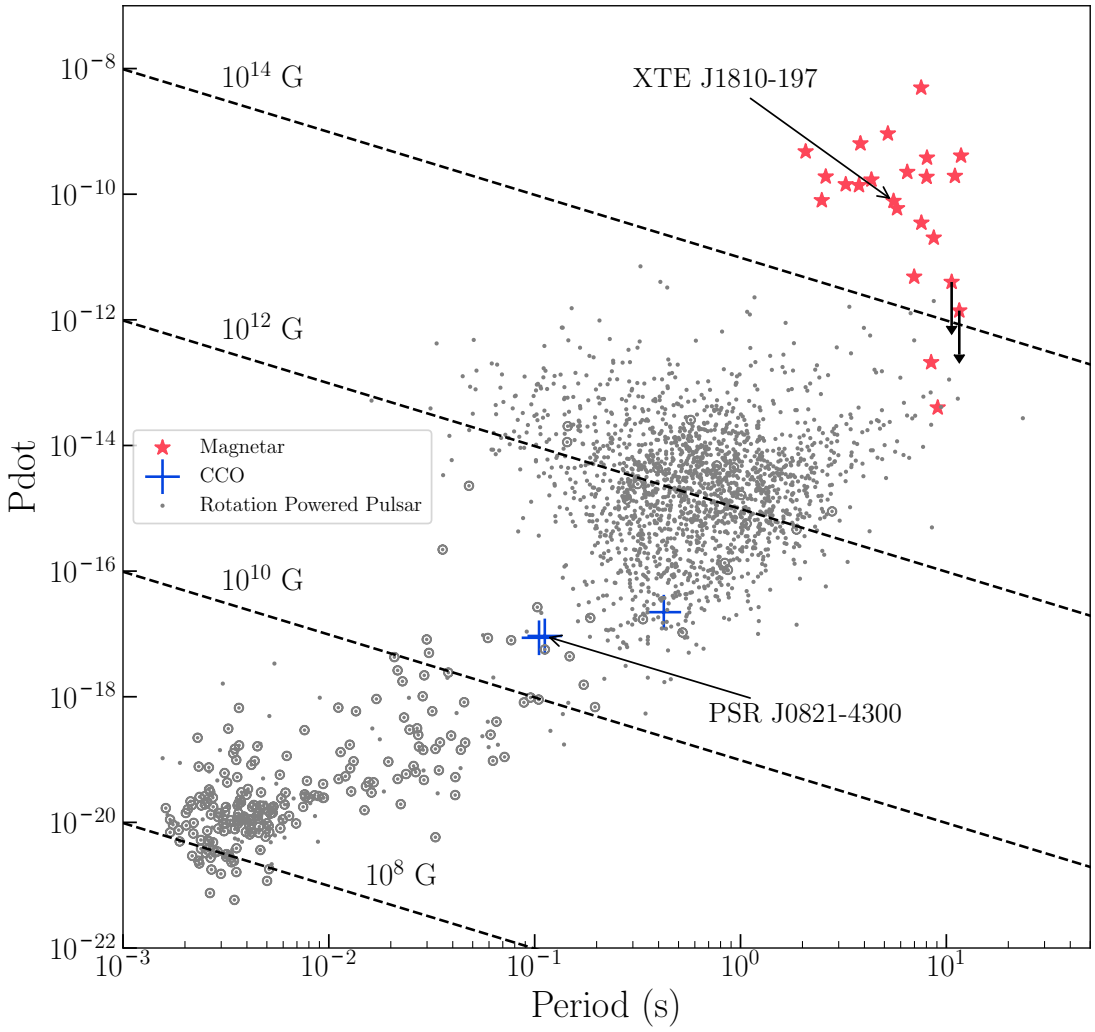


Figure 1.1: The $P$ $\dot{P}$ diagram of pulsars, including magnetars, central compact objects, and rotation powered pulsars. The three CCOs with known periods and period derivatives marked with blue plus signs. All confirmed magnetars in the McGill Magnetar Catalog with known periods and period derivatives are shown as red stars (http://www.physics.mcgill.ca/ pulsar/magnetar/main.html). The rotation powered pulsar data was obtained from the ATNF Pulsar Catalogue. (http://www.atnf.csiro.au/research/pulsar/psrcat/) Note that this plot includes data from millisecond pulsars in globular clusters, whose Pdot values may differ significantly from their intrinsic values due to large accelerations.

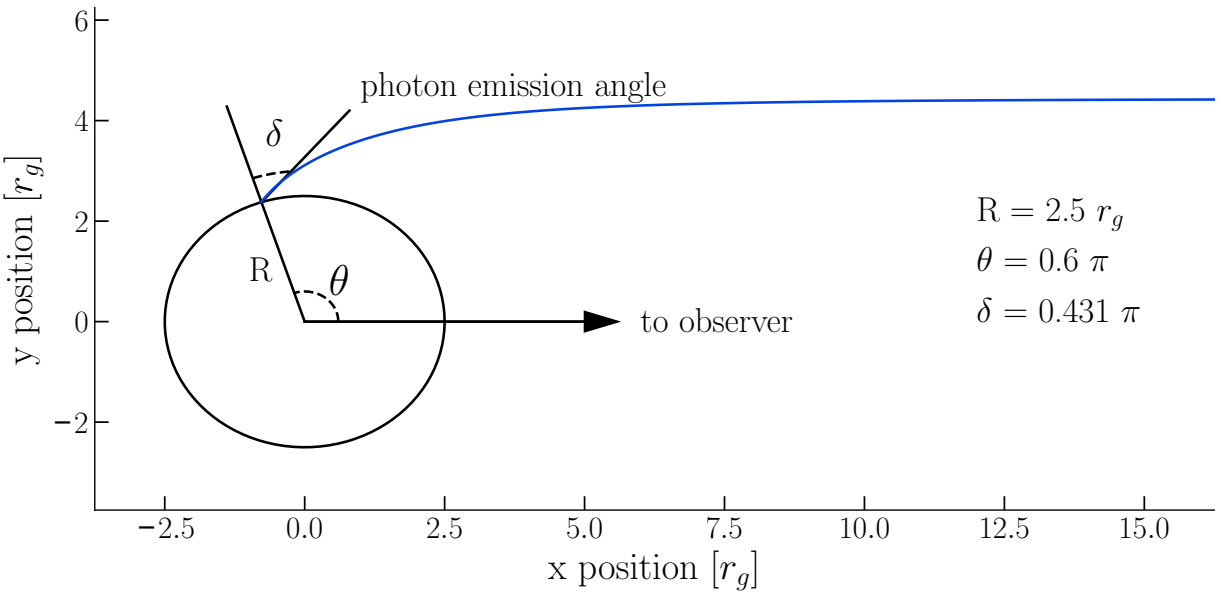


Figure 1.2: Geometry of the angles $\theta$ and $\delta$, which give the magnitude of the light bending. An example photon trajectory is shown for a photon emitted at colatitude $\theta = 0.6\pi$ from the surface of a neutron star at an angle $\delta = 0.431\pi$ with respect to the surface normal. The neutron star in this example has a radius equal to 2.5 $r_g$.

# Chapter 2

# Do Central Compact Objects Have Carbon Atmospheres?

While the chemical composition of central compact object atmospheres is currently unknown, it is expected that the composition of a NS atmosphere can change over time through several processes. These processes include accretion, spallation and diffusive nuclear burning (DNB). Chang & Bildsten (2003) calculated the timescales of these competing processes and developed the theory of DNB. Accretion of circumstellar material and spallation will tend to increase the fraction of hydrogen and helium in the atmosphere. The amount of atmospheric material needed to change the spectrum of a NS is very small ( $10^{20}$M ), and it is impossible to measure such small accretion rates directly. In contrast, DNB can decrease the hydrogen and helium fraction via nuclear fusion into heavier elements such as carbon and oxygen. Since DNB is more efficient at higher temperatures, it is expected to be most effective in younger neutron stars, such as CCOs, because of their relatively high surface temperatures. While the rates of nuclear burning in a neutron star atmosphere with

This section contains text from an article, Alford and Halpern 2020, in preparation for submission to The Astrophysical Journal.

a given composition and temperature is well understood, the rate of accretion of hydrogen onto a neutron star inside a supernova remnant is uncertain. The chemical composition of CCO atmospheres must be determined through observations.

Figure 2.1 shows a comparison between the spectrum of a neutron star with a carbon atmosphere, a hydrogen atmosphere, and a neutron star with a blackbody spectrum. Both magnetic and non-magnetic models are shown. In the following analysis we will be considering only non-magnetic carbon atmosphere models, because these are the models that have been claimed to be applicable to CCOs, where magnetic effects are likely negligible. The spectra are calculated for a 1.4 M  neutron star with a 10 km radius, at a distance of 1 kpc. At a given effective temperature, i.e. given two spectra with the same bolometric luminosity, the blackbody flux dominates at lower energies and the carbon atmosphere flux dominates at higher energies. The energy at which the blackbody spectrum and carbon atmosphere spectrum have the same specific intensity is set by the ratio of photon absorption and scattering processes in the NS atmosphere. Photon scattering processes dominate in the lower energy part of the spectrum and processes where photons are truly destroyed (e.g. bound-bound and bound-free transitions) dominate in the higher energy part of the NS atmosphere spectrum. When these processes are approximately equal, the NS atmosphere flux is approximately equal to the flux of a blackbody with the same effective temperature. For more details on the non-magnetic carbon atmosphere model used in this work see Suleimanov et al. (2014) and Suleimanov et al. (2016). Because the non-magnetic carbon atmosphere spectrum is harder than a blackbody with the same effective temperature, a blackbody model fitted to a given neutron star spectrum will have a larger effective temperature and smaller emitting area than a non-magnetic carbon atmosphere model fitting to the same data. An effective NS temperature calculated from a fit to a non-magnetic carbon atmosphere model will be a factor $f$ lower than the blackbody temperature $T_{BB} = fT_{\mathsf{carbon}}$, where f is usually in the

1.5 - 3 range, and the implied radius of the uniform temperature carbon atmosphere NS is roughly a factor of $f^2$ larger: $R_{\mathsf{carbon}} \quad f^2 R_{BB}$. The non-magnetic carbon atmosphere spectra are harder than the non-magnetic hydrogen atmosphere spectra, which are harder than the blackbody spectra, so the areas of the implied emitting regions decrease significantly from carbon atmosphere, to hydrogen atmosphere to blackbody spectral models. Though the magnetic carbon atmosphere models are probably not applicable to CCOs, we note that they have spectral shapes and implied emitting regions similar to blackbodies. So, even if magnetic carbon atmosphere models are applicable to CCOs, then the radiation must be coming from only a small fraction of the NS surface, and the conclusion that CCOs don't have uniform temperature surfaces is the same. In practice, the X-ray spectra of several CCOs are consistent with both carbon atmosphere, hydrogen atmosphere and blackbody spectra. In the cases where the spectra are consistent with blackbody spectra, either one or two blackbody components may be required to fit the spectrum.

It has been proposed that the CCO in the Cas A SNR has a single-temperature carbon atmosphere (Ho & Heinke 2009), with the X-ray emission coming from the whole surface of the NS. Subsequently Klochkov et al. (2013) and Klochkov et al. (2016) claimed that two candidate CCOs, in the G353.6  0.7 and G15.9+0.2 supernova remnants, have carbon atmospheres. Most recently, Doroshenko et al. (2018) claimed that the CCO in G330+1.0 must have a single-temperature carbon atmosphere. The only evidence in support of these claims is that the single-temperature carbon atmosphere models are capable of fitting the phase-averaged X-ray spectra with reasonable inferred values of the NS radius, and that models of other atmospheric compositions and blackbody models give radii that are much smaller than a NS radius. On the other hand, it is known that at least three CCOs, (located in the Puppis A, Kes 79, and PKS 1209-51/52 supernova remnants) do not have uniform-temperature surfaces; they have heated surface regions that are significantly smaller than

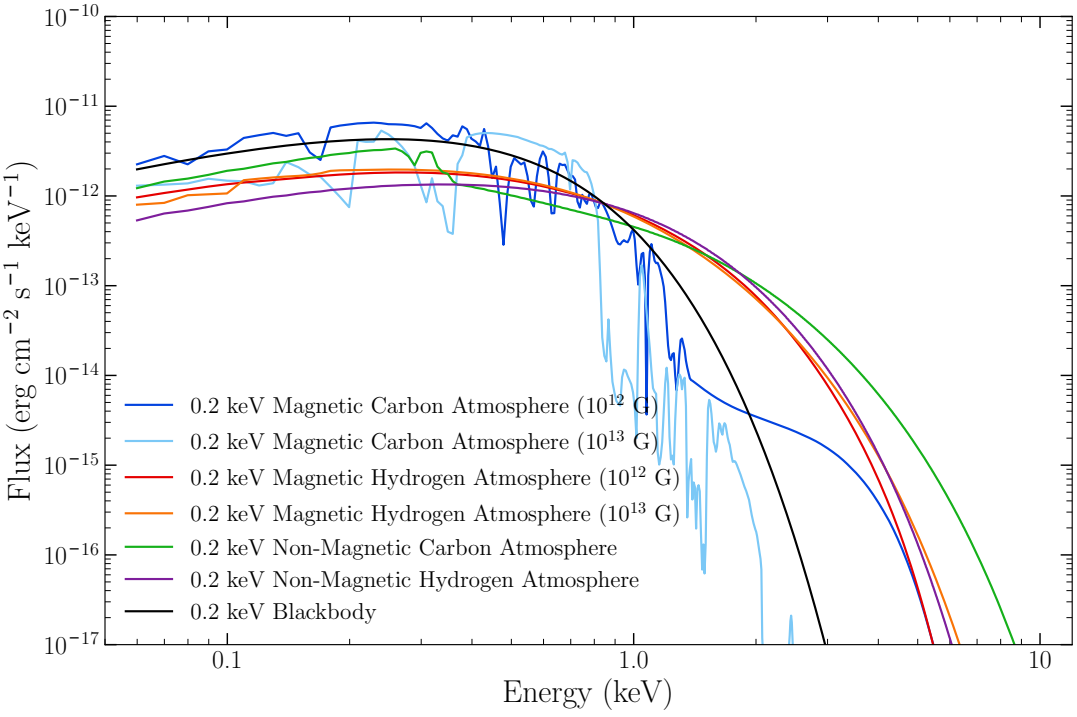


Figure 2.1: The spectrum of neutron star with a carbon atmosphere compared to a blackbody spectrum, and also a hydrogen atmosphere. The non-magnetic carbon atmosphere and non-magnetic hydrogen atmosphere models plotted here are the `carbatm` and `hatm` table models implemented in XSPEC. There are narrow spectral features at low energies in the non-magnetic carbon atmosphere model that are not shown here because their width is much smaller than the energy binning used to construct the table model. Their width is much smaller than the *XMM-Newton* energy resolution. The magnetic hydrogen and carbon models are shown for comparison, and they are computed from the `nsmaxg` model in XSPEC (Mori & Ho 2007; Ho et al. 2008). All spectra have the same effective temperature and therefore the same bolometric luminosity. All models are for a 10 km radius, 1.4 solar mass neutron star at a distance of 1 kpc.

the NS radius (Gotthelf et al. 2013). X-ray pulsations from all of the other CCOs, which would indicate non-uniform surface temperatures, have not been detected.

In this chapter we will first present the results of fitting every CCO to uniform temperature carbon atmosphere models. We will show than some CCOs, known not to have uniform temperature surfaces due to their detected X-ray pulsations, can nevertheless be well fit by a single-temperature carbon atmosphere model with reasonable NS radii at their known distances. We will also show that some CCOs without detected X-ray pulsations cannot have uniform temperature carbon atmospheres because they are at distances too close for this model to be consistent a reasonable NS radius. After gaining these insights from fitting every CCO to a single-temperature carbon atmosphere model, we will calculate new upper limits on the pulsed fractions of several CCO using newly available data. Finally we will present a model the CCOs without detected X-ray pulsation that assumes they have small hot spots. We will calculate the pulsed fractions from this model as a function of the viewing angles and the magnetic inclination angle of the CCOs. We analyze the results of this model and will suggest that many CCOs do have small hot spots, and small amplitude pulsations that are below current limits of detection due to small magnetic inclination angles.

## 2.1 Data Analysis

Here we present the results of X-ray spectral modeling of CCOs with the carbon atmosphere model `carbatm` in XSPEC. This is a four-parameter model that depends on the NS temperature, mass, radius and flux normalization. The flux normalization parameter depends on both the distance to the NS and the fraction of the star surface emitting the radiation. Throughout this paper, we are evaluating the hypothesis that the CCOs have single temperature carbon atmospheres covering their entire surface. Therefore the normalization

parameter is simply a function of the distance to the neutron star. For further details on this model see Suleimanov et al. (2014) and Suleimanov et al. (2017). The size of the regions in the NS distance-radius parameter space quantify how 'easy' it is for the model to describe the data. We will demonstrate that it is possible to fit a single-temperature carbon atmosphere model to most CCOs, including the three CCOs that are known to *not* have single-temperature carbon atmospheres, casting doubt on claimed detection of carbon atmospheres based on this type of spectral modeling alone. All data analysis was performed using XSPEC version 12.9.1, HEASOFT version 6.22 and *XMM-Newton* SAS version 16.1.0, and CIAO version 4.9 with the most recent CALDB version 4.7.5.1. We selected one or more the highest quality observations for each CCO. The specific observation identifiers used for the spectral analyses are listed in Table 2.1.

### 2.1.1 The spectra of most CCOs are, often spuriously, consistent with a single-temperature carbon atmosphere model

Figures 2.2 through 2.11 show the results of spectral fits of all eight confirmed CCOs and two candidate CCOs to the carbon atmosphere model. For most CCOs we have also shown the null hypothesis probability values as contour plots for all plausible values of the NS radius and distance. The independently measured distances are shown as shaded regions. Note that in most of these plots there is some overlap in the regions allowed by the single-temperature carbon atmosphere spectral fitting and the allowed distances and radii. We note that this analysis relies critically on independent measurements of CCO distances. Table 2.2 lists the distances to all CCOs and CCO candidates, along with a description of the measurement methodology. Most distances were estimated using HI velocity measurements.

We found that both CXOU J085201.4  461753 and 1WGA J1713.4  3949 are located at distances too close to have single-temperature carbon atmosphere with reasonable implied

| CCO | SNR | Date | Telescope | Obs. ID |
|---|---|---|---|---|
| RX J0822 4300 | Puppis A | 2009-12-17 | *XMM-Newton* | 0606280101 |
| CXOU J085201.4 461753 | G266.1 1.2 | 2003-05-21 | *XMM-Newton* | 0147750101 |
| ... | ... | 2005-06-02 | *XMM-Newton* | 0207300101 |
| ... | ... | 2010-11-13 | *XMM-Newton* | 0652510101 |
| 1E 1207.4 5209 | PKS 1209 51/52 | 2012-08-11 | *XMM-Newton* | 0679590601 |
| CXOU J160103.1 513353 | G330.2+1.0 | 2015-03-08 | *XMM-Newton* | 0742050101 |
| 1WGA J1713.4 3949 | G347.3 0.5 | 2013-08-24 | *XMM-Newton* | 0722190101 |
| XMMU J172054.5 372652 | G350.1 0.3 | 2007-02-23 | *XMM-Newton* | 0402040101 |
| CXOU J185238.6+004020 | Kes 79 | 2008-10-10 | *XMM-Newton* | 0550670601 |
| CXOU J232327.9+584842 | Cas A | 2006-10-19 | *Chandra* | 6690 |
| XMMU J173203.3 344518 | G353.6 0.7 | 2014-02-24 | *XMM-Newton* | 0722190201 |
| ... | ... | 2007-03-02 | *XMM-Newton* | 0405680201 |
| CXOU J181852.0 150213 | G15.9+0.2 | 2015-07-30 | *Chandra* | 16766 |

Table 2.1: List of CCO X-ray observations analyzed to assess the applicability of the single-temperature carbon atmosphere model. Above the line are the 8 confirmed CCOs and below the line are two candidate CCOs. We selected one or more of the highest quality spectral data sets available for each object. In the case of XMMU J173203.3 344518 we have also analyzed the original *XMM-Newton* observation, Obs. Id 0405680201, cited as evidence of a single-temperature carbon atmosphere, for comparison with the more recent, higher quality observation which is inconsistent with a single-temperature carbon atmosphere model.

NS radii. Nevertheless we are able to fit the spectra of these two CCOs at larger distances. The close distances of these two CCOs implies that they must both have small hots spots and not single-temperature carbon atmospheres. Next we found that we are able to successfully fit the spectra of CXOU J160103.1 513353, XMMU J172054.5 372652 and CXOU J181852.0 150213 to single-temperature carbon atmosphere models, with reasonable values of NS radii resulting. However, the large uncertainties in the distances to these three CCOs leaves open the possibility that they are actually at closer distances and have small hot spots.

Fitting a carbon atmosphere model to the spectrum of 1E 1207.4 5209 required the inclusion of equally spaced absorption features at 0.7, 1.4, 2.1 and 2.8 keV. The features are known to be present in the true two-blackbody spectrum and were required to fit the single-

| CCO | SNR | Distance (kpc) | Method | Ref. |
|---|---|---|---|---|
| RX J0822.0 4300 | Puppis A | 1.3 0.3 | HI Velocity | 1 |
| CXOU J085201.4 461753 | G266.1-1.2 (Vela Jr.) | 0.5-1.0 | X-ray Expansion and Molecular Cloud Association | 2 |
| 1E 1207.4 5209 | PKS 1209 51/52 | $2.1^{+1.8}_{0.8}$ | HI Velocity | 3 |
| CXOU J160103.1 513353 | G330.2+1.0 | >4.9 | HI Velocity | 4 |
| 1WGA J1713.4 3949 | G347.3 0.5 | 1.3 0.4 | HI Velocity | 5 |
| XMMU J172054.5 372652 | G350.1 0.3 | 4.5 | HI and $^{12}$CO | 6 |
| CXOU J185238.6+004020 | Kes 79 | 6.5-7.5 | HI Velocity | 7 |
| CXOU J232327.9+584842 | Cas A | 3.33 0.10 | Optical Expansion | 8 |
| 2XMMi J115836.1 623516 | G296.8 0.3 | 9.6 0.6 | HI Velocity and X-ray HI lower limit | 9 |
| XMMU J173203.3 344518 | G353.6 0.7 | 3.2 0.8 | Association with HII region G353.42 0.37 | 10 |
| CXOU J181852.0 150213 | G15.9+0.2 | 8.5 | X-ray Absorption | 11 |

Table 2.2: CCO distance measurements and measurement methodology. Above the line are eight well-established CCOs. Below the line are three candidates.
References. (1) Reynoso et al. 2017; (2) Allen et al. 2015; (3) Giacani et al. 2000; (4) McClure-Griffiths et al. 2001; (5) Cassam-Chenaï et al. 2004; (6) Gaensler et al. 2008; (7) Giacani et al. 2009 (8) Alarie et al. 2014 (9) Sánchez-Ayaso et al. 2012 (10) Tian et al. 2008 (11) Reynolds et al. 2006

temperature carbon atmosphere model. The absorption features are likely due to quantum oscillations in the free-free opacity in the atmosphere (Suleimanov et al. 2010, 2012). We model the absorption features as gaussian lines with their relative energy spacings held constant, and their strengths and widths allowed to vary to fit the data. The spectrum and single-temperature carbon atmosphere model are shown in Figure 2.9. The distances to 1E 1207.4 5209 allowed by the single-temperature carbon atmosphere model are also about a factor of 2 too large to be compatible with the independent distance estimate. The other two CCOs known to have non-uniform temperature surfaces, CXOU J185238.6+004020 and RX J0822 4300 are also consistent with single-temperature carbon atmosphere models with reasonable NS radii resulting.

Interestingly, we found that the most recent and highest quality *XMM-Newton* observations of XMMU J173203.3 344518 , previously claimed by Klochkov et al. (2013) to have a single-temperature carbon atmosphere, is inconsistent with a single-temperature carbon atmosphere model. Figure 2.11 shows the poor fit to the high quality spectrum and the acceptable fit to the lower quality spectrum previously reported by Klochkov et al. (2013).

Finally, we found that CXOU J232327.9+584842, the original CCO claimed to have a single-temperature carbon atmosphere, is indeed well described by a single-temperature carbon atmosphere model. We note however that the CXOU J232327.9+584842 spectrum is well fit to a single-temperature carbon atmosphere model for a large range of distances, so this spectral fit alone is not convincing evidence of a single-temperature carbon atmosphere.

### 2.1.2 Upper limits on CCO X-ray pulsation amplitudes

Claims that some CCOs have single-temperature carbon atmospheres are based on the assumption that the observed X-ray emission is coming from the entire NS surface. The only evidence in support of this assumption is that X-ray pulsations from these CCOs have not been detected. We can evaluate the strength of this evidence by calculating upper limits on the pulsed fractions of the CCOs without detected pulsations. Gotthelf et al. (2013), in their Table 1, have already reported many upper limits with the data available at that time. Here we will update some of those limits with newly available timing data. The data sets used to search for X-ray pulsations are listed in Table 2.3.

For each pulsation search, we selected photons from a circular region centered on the source. The size of each circular region was chosen to maximize the signal-to-noise ratio $\frac{\mu}{\sigma}$ of the source photons, where $\mu$ is the photon count rate and $\sigma$ is the one sigma uncertainty of the photon count rate. We searched for pulsations from each CCO in two energy bands, one search in the full energy range of the detector, and one search restricted to photons with energies greater than 1.5 keV. This was done to ensure that we do not miss pulsations from a COO that is similar to RX J0822 4300, with pulsations that are almost perfectly out-of-phase in high and low energy bands.

We used the $Z_1^2$ statistic (Buccheri et al. 1983) to search the new datasets for X-ray

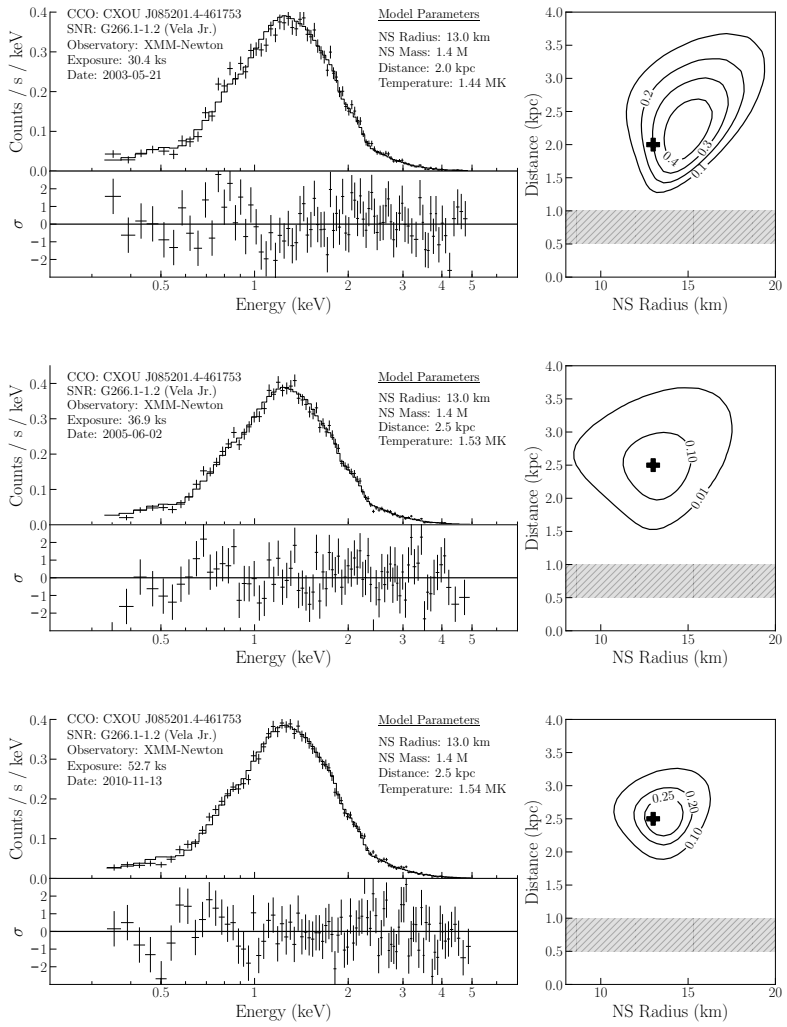


Figure 2.2: Spectra from the three longest *XMM-Newton* observations of CXOU J085201.4 461753 are plotted with along with fits to a single-temperature carbon atmosphere model. The left side of each plot shows the spectrum of CXOU J085201.4 461753 along with a representative single-temperature carbon atmosphere model, with the fit residuals indicated on the bottom panel. On the right side of each plot we show the null hypothesis probability contours for single-temperature carbon atmosphere models with different values of the NS radius and distance. The independently calculated distance range estimates to CXOU J085201.4 461753 is indicated by the gray shaded region. The plus sign indicates the distance and radius values of the single-temperature carbon atmosphere model plotted on the left. All spectra are consistent with the model, with reasonable values of the NS radius, however the implied distances are much larger than the independently derived upper limit. Evidently CXOU J085201.4 461753 does not have a single-temperature carbon atmosphere, and a much smaller thermal emitting region on the NS is required for consistency between the data and the 0.5 - 1.0 kpc distance to CXOU J085201.4 461753.

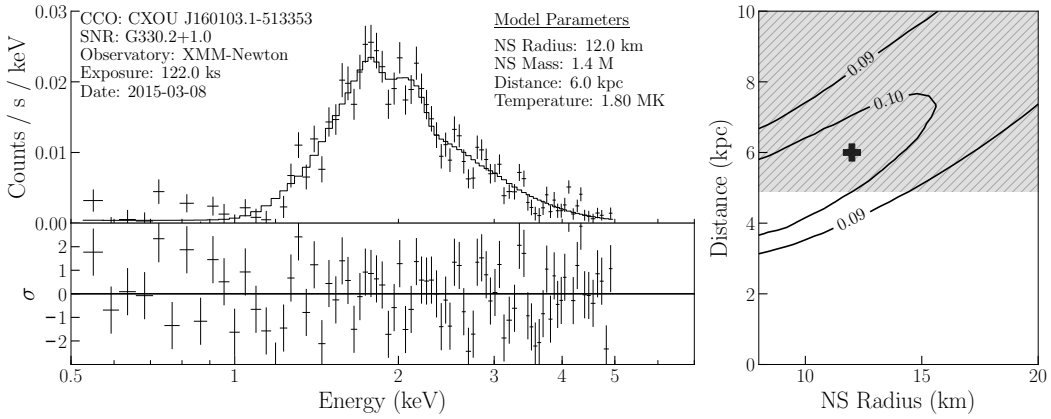


Figure 2.3: Left: The spectrum of CXOU J160103.1 513353 along with a representative single-temperature carbon atmosphere model, with the fit residuals indicated on the bottom panel. Right: The null hypothesis probability contours for single-temperature carbon atmosphere models with different values of the NS radius and distance. The distance range estimate to CXOU J160103.1 513353 is indicated by the gray shaded region. The plus sign indicates the distance and radius values of the single-temperature carbon atmosphere model plotted on the left.

pulsations. The general $Z^2_m$ statistic is defined as

$$Z^2_m = \frac{2}{N} \sum_{k=1}^{m} \left[ \left( \sum_{i=1}^{N} \cos(k\phi_i) \right)^2 + \left( \sum_{i=1}^{N} \sin(k\phi_i) \right)^2 \right] \tag{2.1}$$

where $N$ is the total number of photons and $\phi_i$ are the NS rotational phases calculated from the photon arrival times.

Placing upper limits on the X-ray pulsed fractions of NSs requires knowledge of the probability distributions of power spectra resulting from data containing both a signal and noise. Groth (1975) calculated these probability distributions and gave analytic formulas for the probability $p_n$ that a time series with signal power $P_s$ will have a measured power $P$:

$$p_n(P; P_s) = (P/P_s)^{(n\ \ 1)/2} \exp[\ \ (P + P_s)] I_{n\ \ 1}(2\sqrt{(PP_s)}) \tag{2.2}$$

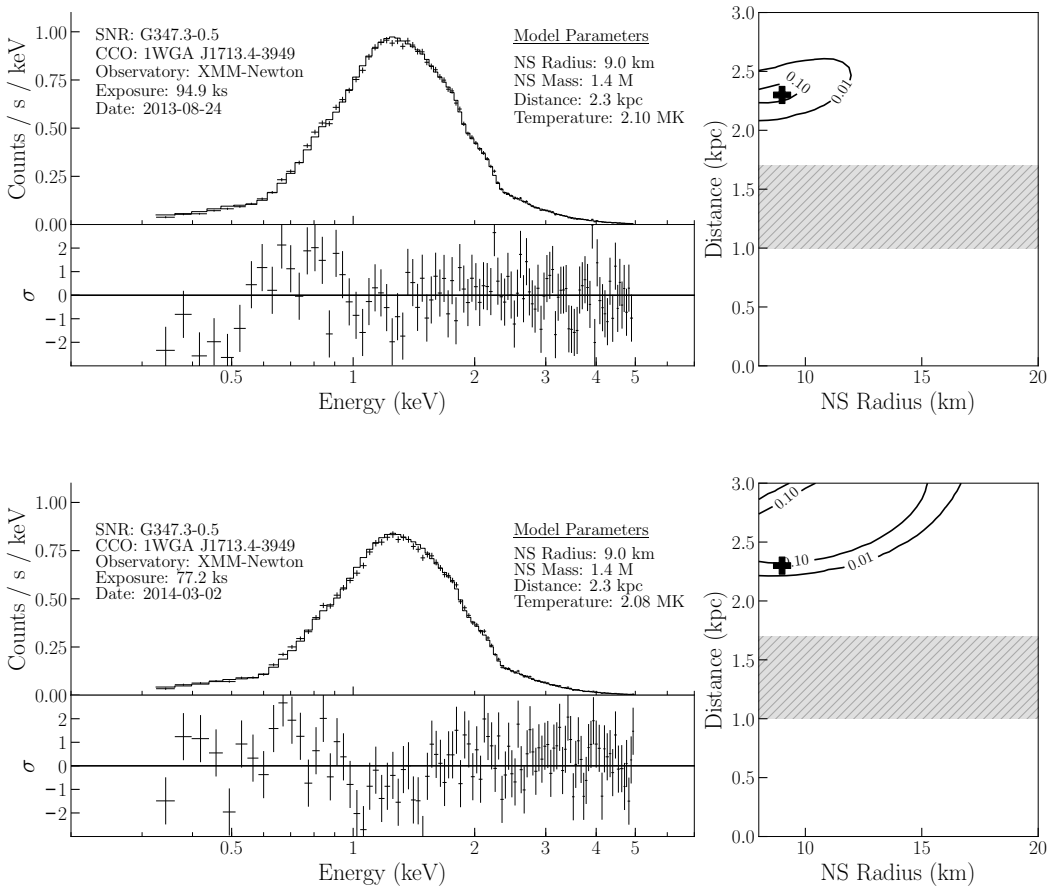


Figure 2.4: Left: The spectrum of 1WGA J1713.4 3949 along with a representative single-temperature carbon atmosphere model, with the fit residuals indicated on the bottom panel. Right: The null hypothesis probability contours for single-temperature carbon atmosphere models with different values of the NS radius and distance. The distance range estimate to 1WGA J1713.4 3949 is indicated by the gray shaded region. The plus sign indicates the distance and radius values of the single-temperature carbon atmosphere model plotted on the left.

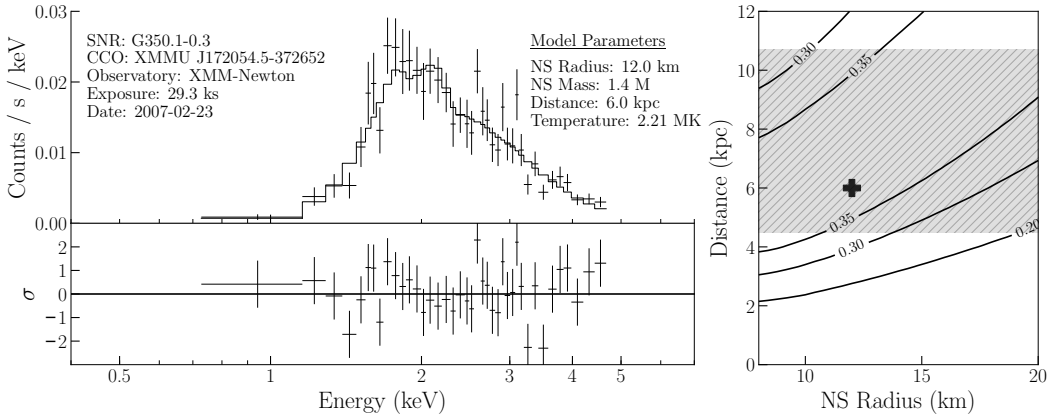


Figure 2.5: Left: The spectrum of XMMU J172054.5 372652 along with a representative single-temperature carbon atmosphere model, with the fit residuals indicated on the bottom panel. Right: The null hypothesis probability contours for single-temperature carbon atmosphere models with different values of the NS radius and distance. The distance range estimate to XMMU J172054.5 372652 is indicated by the gray shaded region. For this figure we have adopted the full 4.5-10.7 kpc distance estimate measured by Gaensler et al. (2008), although those authors argue that XMMU J172054.5 372652 is likely closer to 4.5 kpc. The plus sign indicates the distance and radius values of the single-temperature carbon atmosphere model plotted on the left.

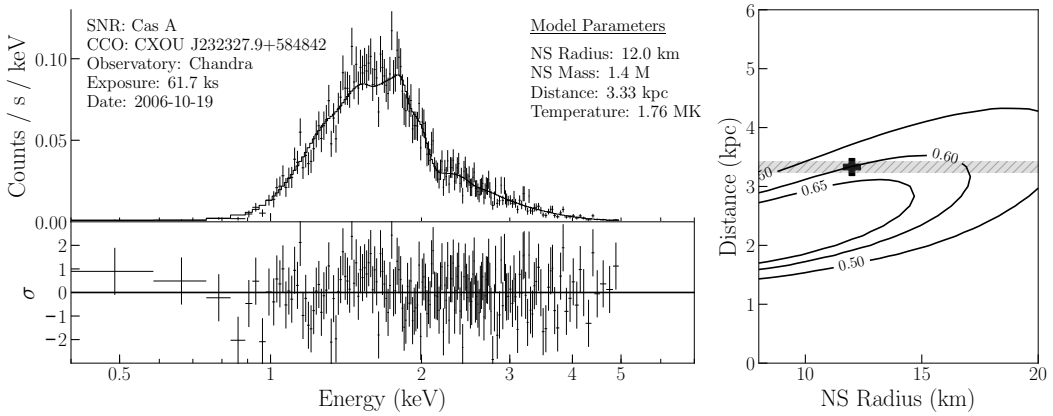


Figure 2.6: Left: The spectrum of CXOU J232327.9+584842 along with a representative single-temperature carbon atmosphere model, with the fit residuals indicated on the bottom panel. Right: The null hypothesis probability contours for single-temperature carbon atmosphere models with different values of the NS radius and distance. The distance range estimate to CXOU J232327.9+584842 is indicated by the gray shaded region. The plus sign indicates the distance and radius values of the single-temperature carbon atmosphere model plotted on the left.

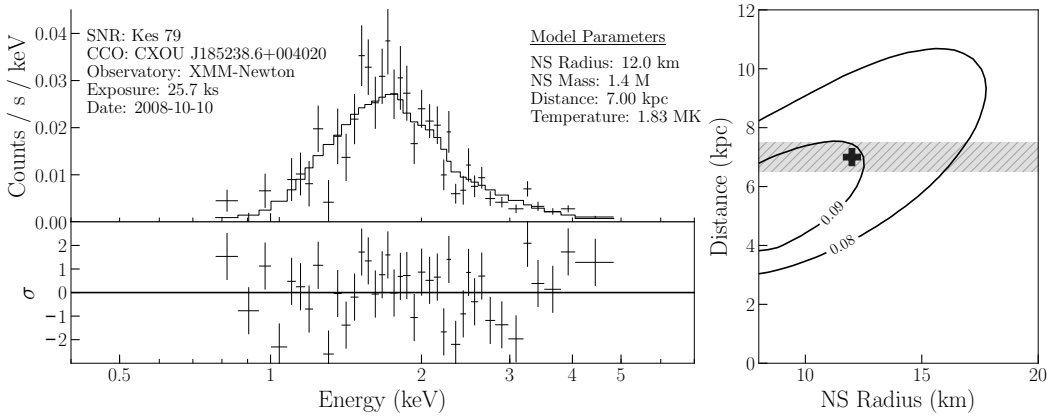


Figure 2.7: Left: The spectrum of CXOU J185238.6+004020 along with a representative single-temperature carbon atmosphere model, with the fit residuals indicated on the bottom panel. Right: The null hypothesis probability contours for single-temperature carbon atmosphere models with different values of the NS radius and distance. The distance range estimate to CXOU J185238.6+004020 is indicated by the gray shaded region. The plus sign indicates the distance and radius values of the single-temperature carbon atmosphere model plotted on the left.

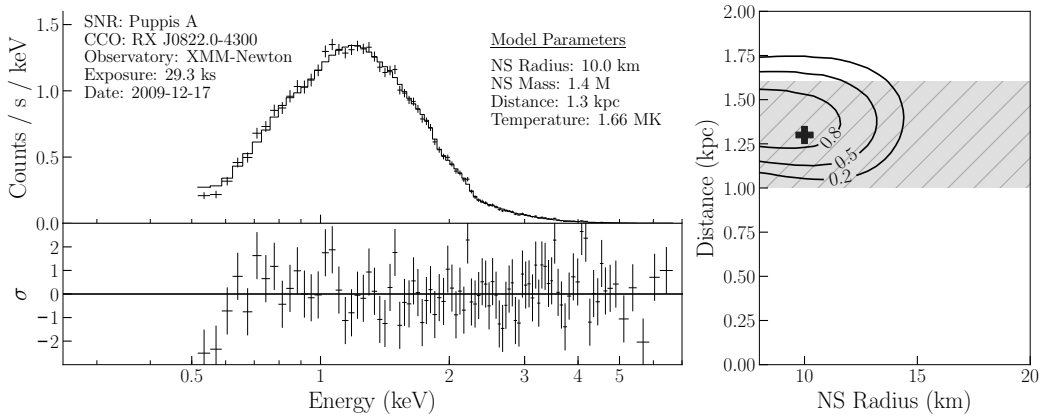


Figure 2.8: Left: The spectrum of RX J0822 4300 along with a representative single-temperature carbon atmosphere model, with the fit residuals indicated on the bottom panel. Right: The null hypothesis probability contours for single-temperature carbon atmosphere models with different values of the NS radius and distance. The distance range estimate to RX J0822 4300 is indicated by the gray shaded region. The plus sign indicates the distance and radius values of the single-temperature carbon atmosphere model plotted on the left.

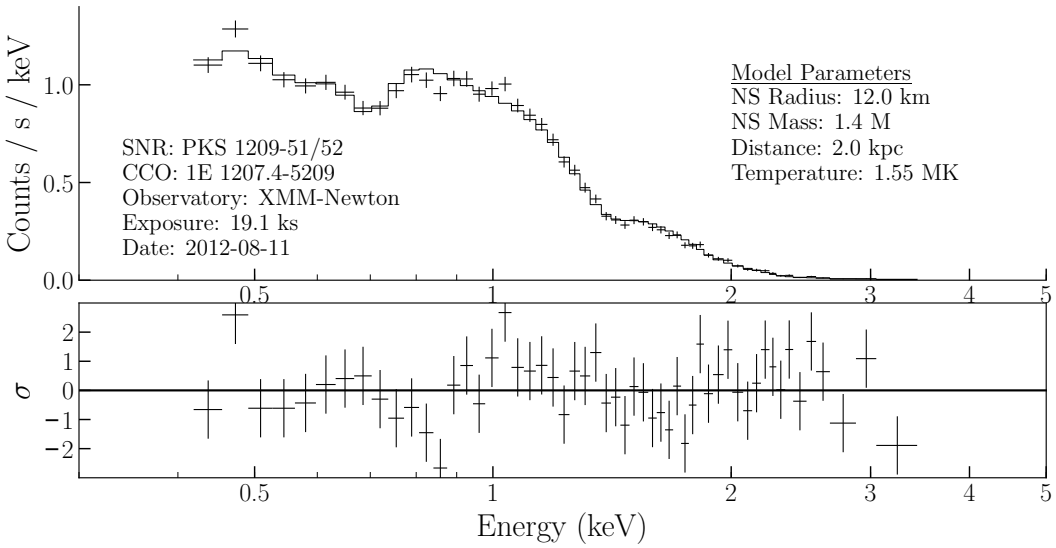


Figure 2.9: The spectrum of 1E 1207.4 5209 along with a representative single-temperature carbon atmosphere model, with the fit residuals indicated on the bottom panel. We have included equally spaced absorption lines in the single-temperature carbon atmosphere model, at 0.7, 1.4, 2.1 and 2.8 keV.

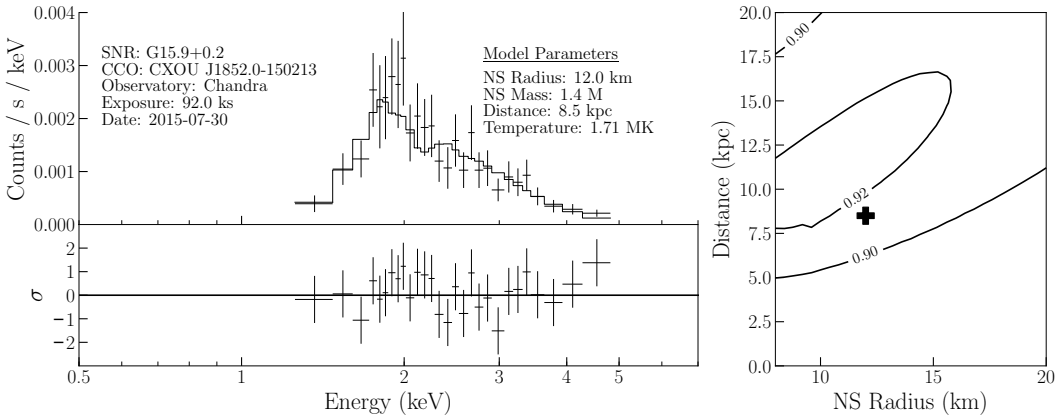


Figure 2.10: Left: The spectrum of CXOU J181852.0 150213 along with a representative single-temperature carbon atmosphere model, with the fit sresiduals indicated on the bottom panel. Right: The null hypothesis probability contours for single-temperature carbon atmosphere models with different values of the NS radius and distance. The distance to CXOU J181852.0 150213 is very uncertain, so we have not plotted any estimated distance range. The plus sign indicates the distance and radius values of the single-temperature carbon atmosphere model plotted on the left. While the spectral model shown here is for a 8.5 kpc distance, as estimated by Reynolds et al. (2006), we note that the available data can accommodate a large range of possible distances.

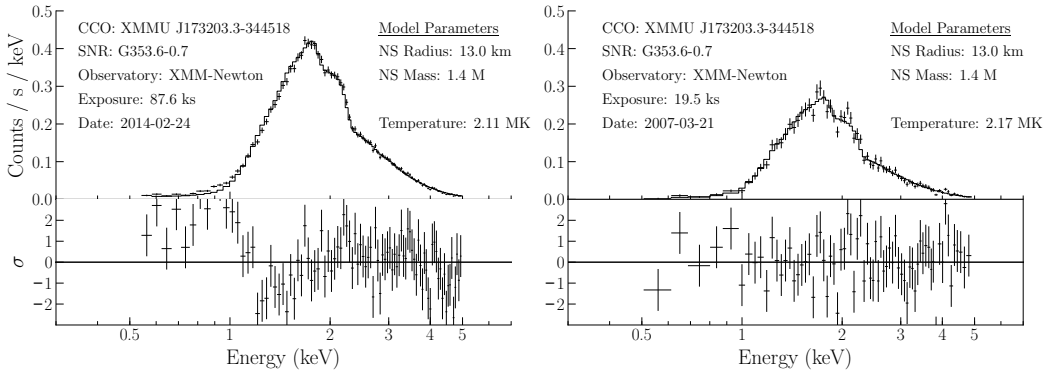


Figure 2.11: Left: The highest quality available X-ray spectrum of CXOU J160103.1 513353 along with a representative single-temperature carbon atmosphere model. Note that the poor fit statistics rule out the single-temperature carbon atmosphere model. Right: The spectrum of CXOU J160103.1 513353 measured in an earlier, much shorter *XMM-Newton* observation. While Klochkov et al. (2013) correctly identified this particular spectrum as consistent with a single-temperature carbon atmosphere model, we consider this unlikely given the much higher quality data now available.

| SNR | Obs. ID | Date | Exp. | Telescope/Instr./Mode | Aperture | Counts | Max. $Z_1^2$ |
|---|---|---|---|---|---|---|---|
| **G266.1 1.2** | | | | | | | |
| | 0147750101 | 2003-05-21 | 58.0 ks | *XMM*/EPIC-pn/SW | $20^{\prime\prime}$ ($22.^{\prime\prime}5$) | 17922 (8278) | 34.3 (38.8) |
| | 0207300101 | 2005-06-02 | 53.9 ks | *XMM*/EPIC-pn/SW | $17.^{\prime\prime}5$ ($32.^{\prime\prime}5$) | 19113 (9378) | 35.2 (32.7) |
| | 0652510101 | 2010-11-13 | 84.5 ks | *XMM*/EPIC-pn/SW | $22.^{\prime\prime}5$ ($27.^{\prime\prime}5$) | 31390 (13604) | 37.1 (36.5) |
| **G330.2+1.0** | | | | | | | |
| | 0500300101 | 2008-03-20 | 68.4 ks | *XMM*/EPIC-pn/SW | $12.^{\prime\prime}5$ ($15.^{\prime\prime}0$) | 2210 (1437) | 31.9 (30.9) |
| | 0742050101 | 2015-03-08 | 140.9 ks | *XMM*/EPIC-pn/FW | $15.^{\prime\prime}0$ ($15.^{\prime\prime}0$) | 4518 (3861) | 32.9 (33.6) |
| **G347.3 0.5** | | | | | | | |
| | 0722190101 | 2013-08-24 | 138.9 ks | *XMM*/EPIC-pn/SW | $37.^{\prime\prime}5$ ($37.^{\prime\prime}5$) | 127751 (59536) | 40.4 (35.6) |
| | 0740830201 | 2014-03-02 | 140.8 ks | *XMM*/EPIC-pn/SW | $37.^{\prime\prime}5$ ($37.^{\prime\prime}5$) | 102660 (47948) | 34.5 (34.4) |
| **G350.1 0.3** | | | | | | | |
| | 14806 | 2013-05-11 | 89.7 ks | *Chandra*/ACIS-S/CC | 1 ACIS-S pixel column | 4561 (4260) | 35.6 (32.5) |
| **Cas A** | | | | | | | |
| | 1857 | 2000-10-04 | 48.9 ks | *Chandra*/HRC-S | $1.^{\prime\prime}2$ | 1455(1122) | 32.3 (35.8) |
| | 1038 | 2001-09-19 | 50.4 ks | *Chandra*/HRC-S | $1.^{\prime\prime}2$ | 1405(1037) | 34.5 (33.7) |
| | 10227 | 2009-03-20 | 132.4 ks | *Chandra*/HRC-S | $1.^{\prime\prime}2$ | 3332(2636) | 36.5 (33.4) |
| | 10229 | 2009-03-24 | 49.0 ks | *Chandra*/HRC-S | $1.^{\prime\prime}2$ | 1243(957) | 35.5 (36.1) |
| | 10892 | 2009-03-26 | 125.7 ks | *Chandra*/HRC-S | $1.^{\prime\prime}2$ | 3236(2599) | 34.6 (33.2) |
| | 10228 | 2009-03-28 | 131.0 ks | *Chandra*/HRC-S | $1.^{\prime\prime}2$ | 3192(2538) | 33.3 (35.4) |
| | 10698 | 2009-03-31 | 52.0 ks | *Chandra*/HRC-S | $1.^{\prime\prime}2$ | 1352(1078) | 38.7 (34.6) |
| **G353.6 0.7** | | | | | | | |
| | 0722190201 | 2014-02-24 | 131.2 ks | *XMM*/EPIC-pn/SW | $37.^{\prime\prime}5$ ($37.^{\prime\prime}5$) | 67241 (53305) | 36.6 (32.3) |

Table 2.3: List of CCO X-ray observations analyzed to search for pulsations and place upper limits on their pulsed fractions. Photons were selected from circular apertures with radii calculated to maximize signal-to-noise ratios. The ACIS-S detector records a one-dimensional image when operated in CC mode. Photons were selected from the column centered on the CCO, and background rates were estimated from the two columns located three pixels away on either side of the CCO column. SW and FW indicate the Small Window mode and Full Window mode of the *XMM-Newton* EPIC-pn detector. Values in parentheses refer to the searches that were restricted to photons with energies greater than 1.5 keV. Observations were searched individually and the power spectra were added to calculate pulsed fraction upper limits.

$I_{n\ 1}$ is the modified Bessel function of the first kind, and the integer n is the number of frequency bins being summed to calculate the total measured power $P$. In this analysis we will be summing power spectra calculated from multiple observations, so n is the number of summed power spectra. We note that there is a factor of 2 difference in the definition of $Z_1^2$ and the measured pulsed power P in the formula above. In Figure 2.12 we plot the probability densities of measured $Z_1^2$ for various intrinsic values of $Z_1^2$ (i.e. values of $Z_1^2$ that would be measured is there was only signal and zero noise), and also for different values of n. We integrate this probability density $p_n$ to calculate $f_n$, the probability that the total measured power is between 0 and P.

| CCO | SNR | Pulsed Fraction (%) |
|---|---|---|
| CXOU J085201.4 461753 | G266.1-1.2 (Vela Jr.) | $< 5$ ($< 7$) |
| CXOU J160103.1 513353 | G330.2 + 1.0 | $< 50(49)$ [$< 25(25)$] |
| 1WGA J1713.4-3949 | G347.3-0.5 | $< 3$ ($< 4$) |
| XMMU J172054.5 372652 | G350.1-0.3 | $< 21(21)$ |
| CXOU J232327.9 + 584842 | Cas A | $< 10(12)$ |
| 2XMMi J115836.1 623516 | G296.8-0.3 | ... |
| XMMU J173203.3 344518 | G353.6-0.7 | $< 5$ ($< 6$) |
| CXOU J1852.0 150213 | G15.9 + 0.2 | ... |

Table 2.4: Most current upper limits on the pulsed fraction of CCOs without detected X-ray pulsations. We list the upper limits for the full energy range and then the upper limits for energies greater than 1.5 keV in parentheses. With the exception of CXOU J160103.1-513353, these limits are for searches down to at least 12 ms periods. The pulsed fraction upper limit for CXOU J160103.1-513353 is $< 50\%$ for all plausible CCO periods down to 12 ms, and $< 25\%$ for periods greater than 146 ms (the Nyquist limit of the *XMM-Newton* pn detector in Full Window mode). The upper limit for Cas A was calculated in Halpern & Gotthelf (2010).

$$f_n(P; P_s) = \int_0^P p_n(x; P_s)\mathrm{dx} \tag{2.3}$$

We calculated upper limits on intrinsic pulsed fractions by using this probability distribution together with the peak $Z_1^2$ found in a period search to compute the 99% confidence level of a pulse detection. We then computed the corresponding pulsed fraction, $f_p$, using a relationship between pulsed fraction, $Z_1^2$ and the number of X-ray counts $N$, derived in Pavlov et al. (1999) for the special case of sinusoidal signals:

$$f_p = (1 + N_b/N_s)\sqrt{2Z_1^2/N} \tag{2.4}$$

For an observation of length $T$ and time resolution $\delta t$, the smallest measurable frequency is $f_{min}$ $1/T$, and the largest measurable frequency is the critical, or Nyquist, frequency $f_c$ $1/2\delta t$. The number of independent Fourier frequencies is equal to $T(f_c$ $f_{min})$. In

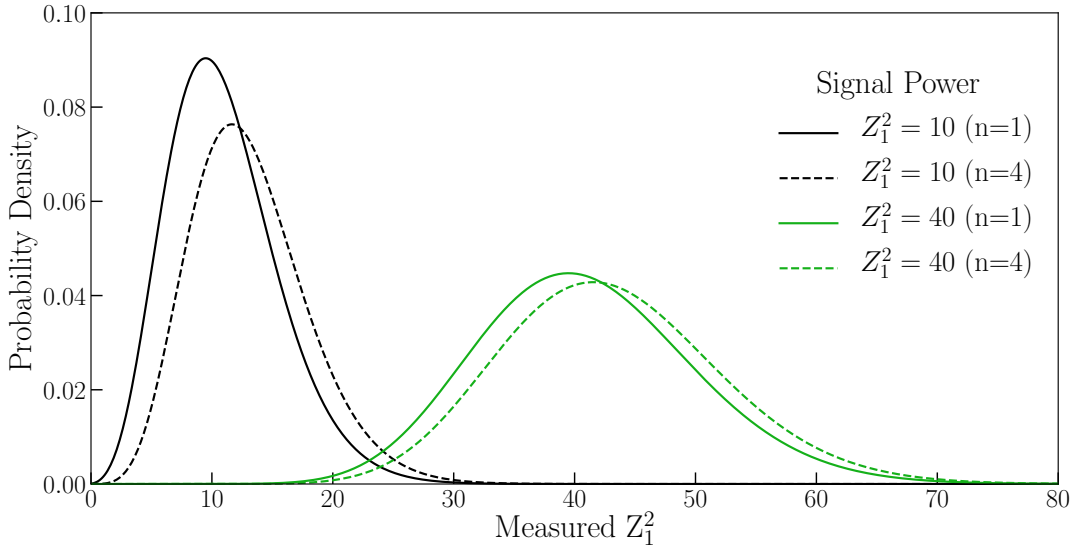


Figure 2.12: Probability densities of measured $Z_1^2$ for various intrinsic values of $Z_1^2$ and the number of combined power spectra bins n.

practice, a periodicity search will miss a peak in the $Z_1^2$ statistic when the peak occurs between two independent Fourier frequencies. This is particularly important for the detection of weak signals. To ensure that we do not miss a signal in between two independent Fourier frequencies, we oversampled the independent frequencies by a factor of at least 5 in all of our searches. This oversampling, while necessary, would complicate our calculation of the upper limits on the CCO pulsed fractions if we used the maximum $Z_1^2$ from the oversampled searches. To remedy this, we use only the $Z_1^2$ maxima from the independent Fourier frequencies to compute pulsed fraction upper limits. When searching for pulsations in multiple observations, we added the power spectra, and used the peak $Z_1^2$ from the total power spectrum to calculate the upper limits on the pulsed fractions.

Table 2.4 list the results of this timing analysis. We can conclude from the now updated set of pulsed fraction upper limits, that the CCO in Kes 79 is an outlier, i.e. that none of the other confirmed CCOs have similarly large pulsed fractions of 64%. The only caveat

is CXOU J160103.1-513353: the pulsed fraction upper limit for CXOU J160103.1-513353 is $< 50\%$ for all plausible CCO periods down to 12 ms, and $< 25\%$ for periods greater than 146 ms (the Nyquist limit of the *XMM-Newton* pn detector in Full Window mode)

## 2.2 Do most CCOs have small hots spots and small magnetic inclination angles?

We will now consider the possibility that the CCOs without detected X-ray pulsations actually do have hot spots, and the amplitudes of their pulsations are simply below the current limits of detectability. Small pulsation amplitudes can be attributed to either: 1) a small angle $\Psi$ between the rotation axis and the observers line of sight, or 2) a small magnetic inclination angle $\zeta$, i.e. the angle between the rotation axis and the hot spot pole. By using the term 'magnetic inclination angle', we are implicitly assuming that the hot spot location on the NS surface aligns with the dipole magnetic field axis. While this is likely the case, in the following calculations we are only interested in the locations of hot spots relative to the NS rotation axis, regardless of whether or not the hot spot axes are in fact the dipole magnetic field axes. Rotation vector angles $\Psi$ are certainly sinusoidally distributed among CCOs because it is the sinusoidal distribution that one would obtain from randomly selecting a 3d rotation vector and a 3d vector pointing from the star toward the observer. Previous authors have also assumed that the distribution of magnetic inclination angles is also sinusoidal, i.e. it is the distribution that one would obtain from randomly selecting a 3d rotation vector and a 3d magnetic axis vector (Suleimanov et al. 2017). If this is the true magnetic inclination angle distribution, then orthogonal rotators are much more common than configurations where the magnetic axis and spin axis are approximately parallel. However, there is no reason to expect a sinusoidal distribution of CCO $\zeta$ values, and in fact there there is

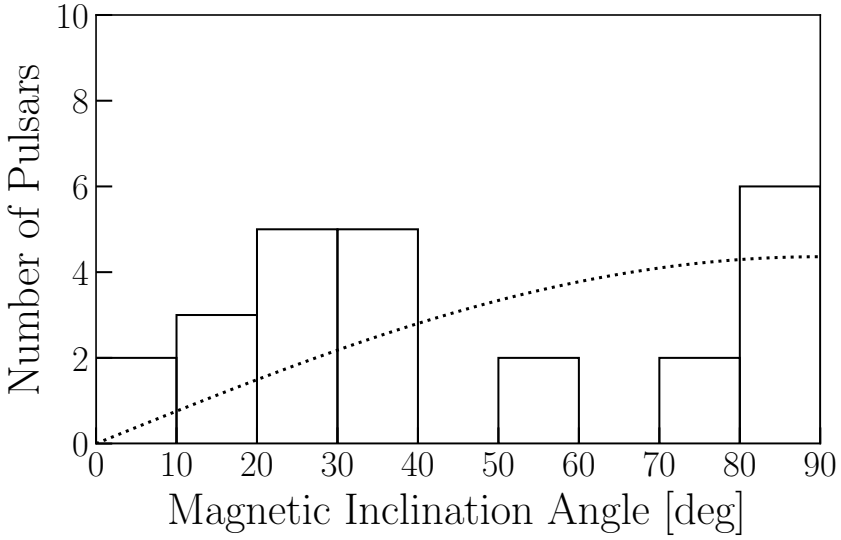


Figure 2.13: Empirical distribution of magnetic inclination angles for young gamma-ray pulsars versus a sinusoidal distribution. There is an overabundance of pulsars with small magnetic inclination angles, and an under abundance of pulsars with intermediate magnetic inclination angle values. Adapted from Figure 29 in Rookyard et al. (2015a).

empirical evidence that the magnetic inclination angles of other classes of neutron stars are biased toward small angles. Rookyard et al. (2015b) analyzed a small sample of gamma-ray pulsars and found a that the magnetic inclination angles were inconsistent with a sinusoidal distribution, with more small inclination angles than would be expected, as shown in Figure 2.13. Perhaps more convincingly, Tauris & Manchester (1998) analyzed the distributions of more than three hundred radio pulsar magnetic inclination angles, calculated from radio polarization studies. They found that, after considering various selection effects, the population of radio pulsars seems consistent with a cosine-like distribution, biased toward small magnetic inclination angles. It thus seems plausible that the CCOs may also have a distribution of magnetic inclination angles that is biased toward small values. We will show below that the CCO $\zeta$ distribution must be even more biased toward small values, in order to be consistent with the strong pulsed fraction upper limits we have calculated for CCOs.

For each CCO without detected X-ray pulsations we fit the spectrum to a simple blackbody model and calculate the size of two antipodal hot spots. For the all of these calculation we assume a 12 km radius and 1.4 M  neutron star. We find that in most cases the angular radii of the two antipodal hot spots are . 10 degrees. ((1WGA J1713.4  3949 is the exception and requires a two blackbody model to fit its spectrum). This is well within the limit where the light curves of these hot spots can be approximated by point sources. Therefore the following calculations and conclusions will not change if we model the spectra with slightly different distances or hydrogen atmosphere models, since light curves produced by the hot spots would still be within the point like approximation as long as the angular radii are . 10 degrees. We also emphasize that the known population of CCOs is relatively small, and so we are aiming to make only a first order estimate of what the distribution of CCO magnetic inclination angles looks like.

Figure 2.14 shows the pulsed fractions calculated from this toy model as a function of $\zeta$ and $\Psi$. Since the viewing angle $\Psi$ is certainly sinusoidally distributed, we can conclude that the CCOs without detected pulsations are most likely in the upper left region of the figure, with large values of $\Psi$ and small values of $\zeta$. We next take these pulsed fractions shown in Figure 2.14 and calculate CCO pulsed fraction cumulative distribution functions for several assumed statistical distributions $D(\zeta)$ of $\zeta$. In other words, we are calculating the percentage of CCOs one would expect to have pulsed fractions under a given maximum pulsed fraction $f_p^{max}$, assuming some distribution of $\zeta$. For each $f_p^{max}$ we calculate the probability $p$ that a randomly selected CCO has a pulsed fraction less than $f_p^{max}$:

$$p = \frac{\int_0^{\pi/2}\int_0^{\pi/2} S \sin\psi \, D(\zeta)\, \mathrm{d}\zeta \, \psi}{\int_0^{\pi/2}\int_0^{\pi/2} \sin\psi \, D(\zeta)\, \mathrm{d}\zeta \, \mathrm{d}\psi}, \tag{2.5}$$

where $S(\psi, \zeta)$ is defined as:

$$S(\psi, \zeta) = \begin{cases} 1 & f_p(\psi, \zeta) < f_p^{max} \\ 0 & f_p(\psi, \zeta) > f_p^{max} \end{cases} \tag{2.6}$$

Figure 2.15 shows the results of these calculations. We find that if $\zeta$ was actually uniformly or sinusoidally distributed then a majority of CCOs would have pulsed fractions greater than 10%, in contradiction to what is observed. On the other hand, if $\zeta$ is exponentially distributed with a scale factor of 15 , then is expected that a majority of CCOs will have pulsed fractions $< 10\%$, as is observed. We emphasize that this is a toy model, particularly because we have assumed that the antipodal hot spots are the same size, allowing the pulsations to almost perfectly cancel out in some regions of the $\zeta$ and $\Psi$ parameter space. If the spot were of unequal size, then this would slightly increase the pulsed fractions shown in Figure 2.14, but would not change the main conclusion that $\zeta$ must be approximately exponentially distributed with a scale factor of 10 in order to be consistent with the pulsed fraction upper limit data.

Finally, we consider what physical mechanism may be producing CCOs with small magnetic inclination angles. It has long been known that electromagnetic torques can decrease the inclination angles of neutron stars, with calculations by Michel & Goldwire (1970) showing that these torques can align the rotational and magnetic axes of a neutron star in vacuum on an exponential timescale of millions of years for initial spin periods and dipole magnetic field strengths typical of CCOs. More recently, Philippov et al. (2014) calculated the change in neutron star inclination angles using MHD simulations that include magnetospheric torques, and found that the inclusion of magnetospheric effects decreased the rate of inclination angle change from exponential to a power law. Both of the calculations by Michel & Goldwire (1970) and Philippov et al. (2014) show that electromagnetic and mag-

netospheric torques act too slowly to significantly change the inclination angles of CCOs from their birth values, since CCOs are only hundreds or thousands of years old, as determined by their associations with SNRs. A faster inclination angle alignment mechanism was studied by Dall'Osso & Perna (2017), who found that dissipation of precessional motions by bulk viscosity can produce a bi-modal distribution of inclination angles on  300 year timescales. This mechanism is therefore fast enough to produce small CCO inclination angles. Whether the mechanism produces a large or small inclination angle depends on the NS magnetically-induced ellipticity, mass, radius, and initial spin period, so it may be the case that the values of these parameters applicable to CCOs tend to produce small inclination angles. Interestingly, this mechanism is effective when toroidal fields dominate the poloidal fields, which seems is likely for some CCOs. Alternatively, CCOs may simply be born with small inclination angles due to an as-yet-unknown mechanism.

In the next chapter I will measure the angles $\zeta$ and $\Psi$ of the CCO RX J0822  4300 in the Puppis A supernova remnant. While the results are degenerate with respect to interchange of $\zeta$ and $\Psi$, it turns out there is a $> 90\%$ probability that RX J0822  4300 is in the 'most probable region' of the parameter space labeled in Figure 2.14.

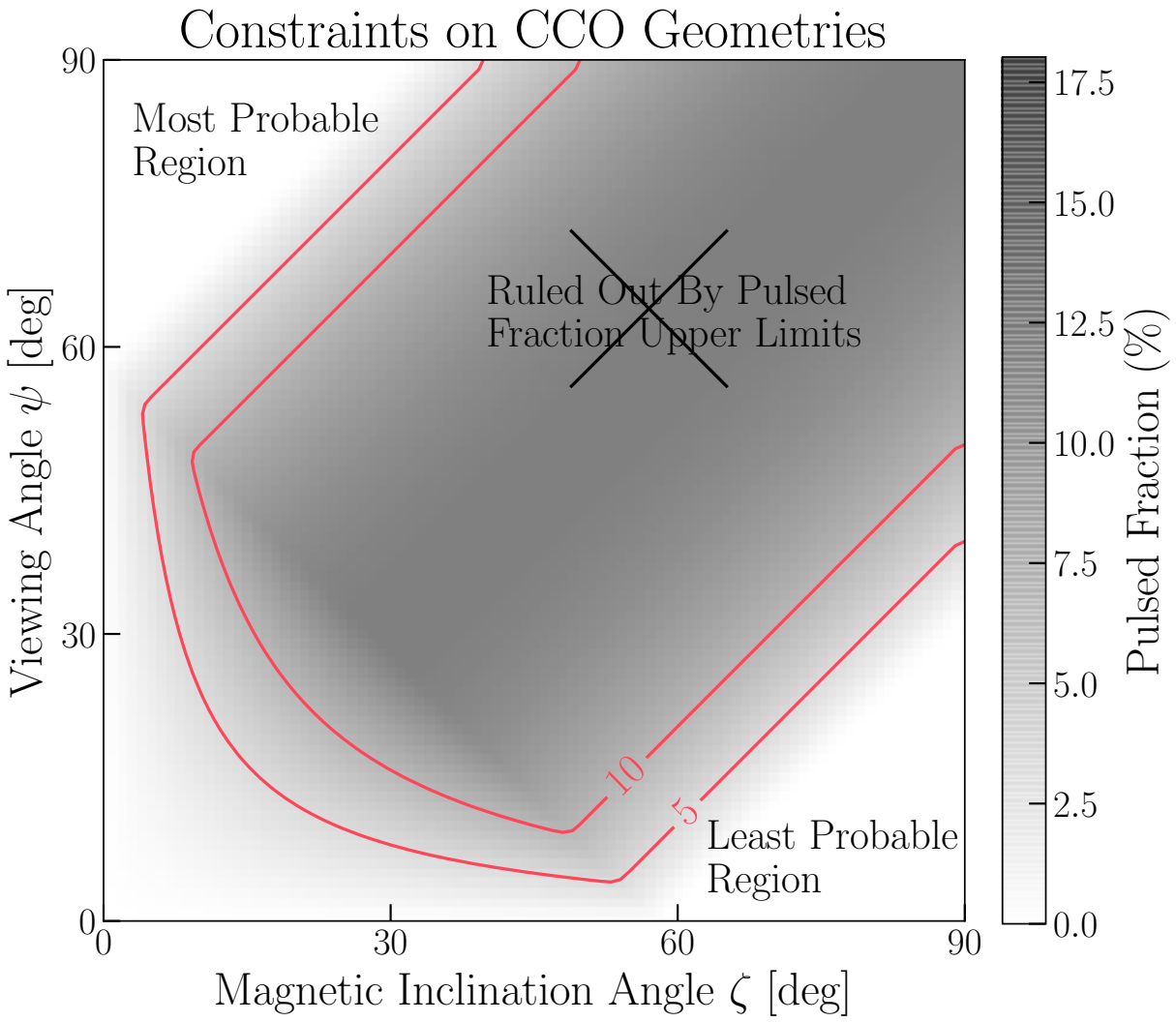


Figure 2.14: Pulsed fractions as a function of the geometric angles $\Psi$ and $\zeta$. We consider 1.4 M , 10 km radius neutron stars with equal temperature antipodal hot spots, and account for the general relativistic effect of light bending when computing the pulsed fractions. The hot spot sizes are functions of the angles $\Psi$ and $\zeta$, but are effectively point-like for the blackbody emission models fitted to the non-pulsing CCOs considered here. If some of the CCOs without detected X-ray pulsations have small hot spots, as opposed to uniform temperature surfaces, then they must be in the region of the parameter space that produces such low amplitude pulsations. Because the CCO viewing angle $\Psi$ is sinusoidally distributed, the most probable region of the parameter space to find these non-pulsing CCOs is in the upper left of the figure.

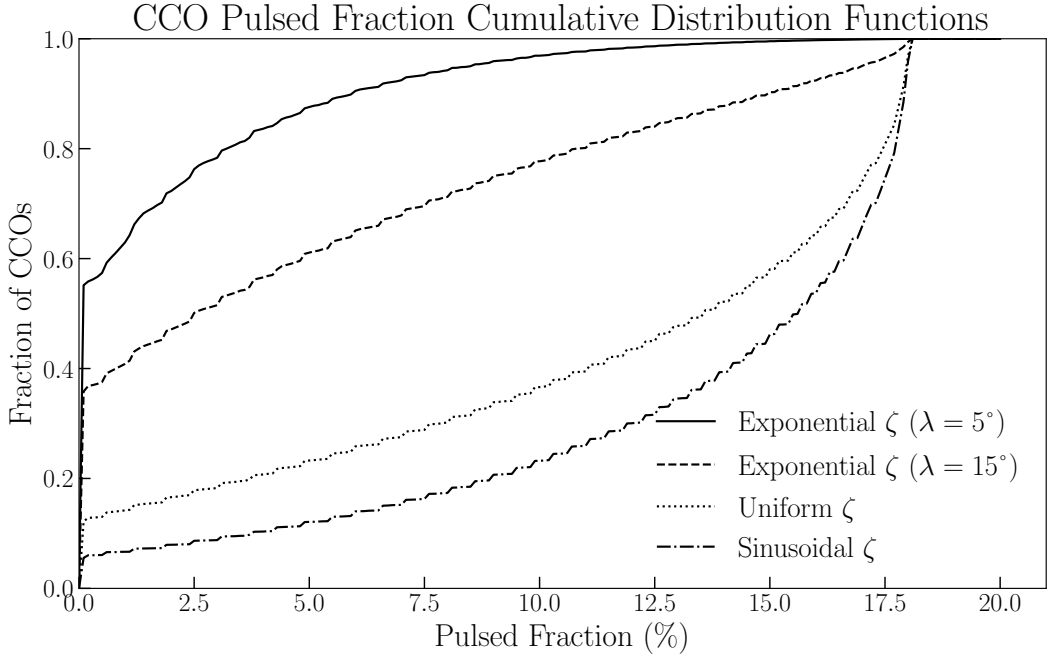


Figure 2.15: CCO pulsed fraction cumulative distribution functions for several assumed distributions of the magnetic inclination angle $\zeta$. These cumulative distribution functions are calculated from the pulsed fractions shown in Figure 2.14, which were calculated from a model with two antipodal spots. Given that some CCOs have hot spots and low ( 5%) upper limits on their pulsed fractions, we can conclude that sinusoidal and uniform $\zeta$ distributions are highly improbable. An exponential distribution of magnetic inclination angles with a scale factor $\lambda$ 5 is consistent with non-detection of several CCOs with small hot spots and very low upper limits on their pulsed fractions. Note that in this toy model the two hot spots have the same angular size, which makes their individual pulsations almost perfectly cancel out in some regions of the parameter space. Relaxing this condition would not substantially change the result that $\zeta$ must be approximately exponentially distributed with a scale factor of 10 in order to be consistent with the pulsed fraction upper limit data.

# Chapter 3

# Modeling the Non-Axial-Symmetric Surface Temperature of the Central Compact Object in Puppis A

## 3.1 Introduction

Central Compact Objects (CCOs) are a class of point-like X-ray sources found in supernova remnants (SNRs). Gotthelf et al. (2013) confirmed the nature of CCOs as "anti-magnetars", i.e. neutron stars born with weak ( $10^{10}$ $^{11}G$) spin-down measured magnetic fields. Observationally, CCOs are characterized by steady thermal X-ray emission, a lack of emission at other wavelengths, and the absence of a surrounding pulsar wind nebula. Three of the eight confirmed CCOs have measured pulsation periods and period derivatives. The X-ray flux from the hot spots of these three neutron stars exceeds their spin-down power, and is likely powered by the residual cooling of these young neutron stars. The CCOs without detected

This section contains text from an article, Alford et al. 2020, in preparation for submission to The Astrophysical Journal.

X-ray pulsations may have similar hot surface regions, that do not modulate the X-ray flux due to unfavorable viewing geometries or lower intrinsic pulse modulation.

RX J0822 4300 was first discovered as an X-ray source near the center of the Puppis A SNR by Petre et al. (1982) analyzing *Einstein* HRI data. *ROSAT* data later confirmed that RX J0822 4300 is an unresolved point source, and therefore likely the compact remnant of the Puppis A progenitor (Petre et al. 1996). RX J0822 4300 is located at distance of 1.3 kpc, near the center of the 4500 year old Puppis A supernova remnant (Reynoso et al. 2017; Becker et al. 2012). To a first approximation, the surface temperature profile of RX J0822 4300 consists of two antipodal hot spots with temperatures of 0.2 keV and 0.4 keV. The area of the hotter spectral component is a factor of 25 times smaller than the area of the cooler component. Since the pulsations from these two hot spots are approximately 180 degrees out of phase, they cancel out in the integrated *XMM-Newton* X-ray band. RX J0822 4300 has $< 20\%$ modulated pulse profiles and a phase reversal at 1.2 keV. The pulse phase reversal makes the X-ray pulsations almost perfectly cancel in the integrated *XMM-Newton* energy band. The 112 ms pulsations were originally discovered by searching high (1.5-4.5 keV) and low (0.5- 1.0 keV) energy bands separately (Gotthelf & Halpern 2009).

In this chapter, we extend the original analysis of Gotthelf et al. (2010) with the benefit of significantly more *XMM-Newton* data. We extend the pulse profile modeling from 3 to 16 energy bands. For the first time, we are able to measure a deviation of the hot spots from an axisymmetric geometry.

## 3.2 Data Reduction and Analysis

This study utilizes the combined EPIC pn data from nineteen *XMM-Newton* observations of RX J0822 4300. A log of these observations is shown in Table 3.1. All were performed in

Table 3.1: Log of *XMM-Newton* Observations

| ObsID | Date | Livetime (ks) | $Z_1^2$ Statistic |
|---|---|---|---|
| 0113020101 | 2001-04-15 | 15.8 | 49.3 |
| 0113020301 | 2001-11-08 | 16.1 | 51.7 |
| 0606280101-A | 2009-12-17 | 29.3 | 79.6 |
| 0606280101-B | 2009-12-17 | 26.6 | 28.4 |
| 0606280201 | 2010-04-05 | 25.3 | 101.6 |
| 0650220201 | 2010-05-02 | 13.6 | 23.7 |
| 0650220901 | 2010-10-15 | 16.4 | 46.2 |
| 0650221001 | 2010-10-15 | 16.3 | 60.7 |
| 0650221101 | 2010-10-19 | 18.6 | 42.5 |
| 0650221201 | 2010-10-25 | 17.2 | 70.2 |
| 0650221301 | 2010-11-12 | 16.5 | 25.7 |
| 0650221401 | 2010-12-20 | 19.0 | 58.2 |
| 0650221501 | 2011-04-12 | 21.0 | 68.2 |
| 0657600101 | 2011-05-18 | 25.6 | 92.3 |
| 0657600201 | 2011-11-08 | 26.1 | 51.1 |
| 0657600301 | 2012-04-10 | 24.7 | 96.8 |
| 0722640301 | 2013-10-29 | 31.9 | 118.2 |
| 0722640401 | 2013-10-31 | 29.0 | 86.2 |
| 0742040201 | 2014-10-18 | 32.1 | 106.0 |
| 0781870101 | 2016-11-08 | 50.2 | 146.9 |

Table 3.2: List of the *XMM-Newton* observations of RX J0822 4300 used in this study. We summed each data set to produce a single combined spectrum and a set of energy dependent pulse profiles. The $Z_1^2$ statistic is calculated in the 1.5-4.5 keV energy band. The observation beginning on 2009-12-17 was split into two separate files in the *XMM-Newton* archive, labeled here as 060628010-A and 060628010-B.

small window mode with the thin filter. Our analysis made use of the most recent version 16.22 of the HEASoft software, as well as of the most recent version xmmsas_20170719_1539-16.1.0 of the *XMM-Newton* SAS software. Observations were reprocessed with the `epchain` pipeline to apply the latest calibration products and clock corrections. The SAS function `barycen` was used to correct photon arrival times to the solar system barycenter. The data sets were filtered to remove time intervals contaminated with particle flares according to the recommended criteria. Standard flag and pattern filters `(PATTERN<=4 && FLAG==0)` were applied.

The source photons were extracted from a circular region with a 30" radius, and the background spectrum was extracted from an annular region with a 32.5" inner radius and 45" outer radius. We verified that larger background regions give consistent spectral results. The size of the source region was chosen to maximize the Rayleigh statistic (Buccheri et al. 1983) in our timing analysis. X-ray pulsations were evident in all observations, and Table 3.1 shows the Rayleigh $Z_1^2$ statistic in the 1.5 - 4.5 keV band for each observation. Pulse profiles from each observation were aligned by fitting the pulses in the 1.5 - 4.5 keV band to a sine wave and then shifting the phase of all photons so that the 1.5 - 4.5 keV band pulses are aligned. The summed pulses in 16 energy bands are shown in Figure 3.6.

Gotthelf & Halpern (2009) found that the spectrum of the CCO in Puppis A shows deviations from a pure two blackbody model. These deviations can be modeled either with the addition of an absorption line at  0.45 keV, or of an emission line at  0.75 keV. We performed a careful analysis to determine the validity of these possible spectral features. The main concerns were that a spectral feature could be an artifact of imperfect background subtraction, or contamination of X-rays from the Puppis A SNR. Contamination from the supernova remnant could occur due to the details of the operation of the pn detector in small window mode. See the Appendix for a discussion of the details of the background charac-

terization and subtraction method. After concluding that the spectral feature is intrinsic to RX J0822 4300 we chose to model it as an emission line, which is a marginally better fit to the phase-averaged spectrum.

### 3.2.1 Emission Model

Our starting point is the emission model originally described in Gotthelf et al. (2010). The observable X-ray emission from RX J0822 4300 can be attributed entirely to the two hot surface regions; the rest of the NS surface is cool enough that it makes no detectable contribution to the X-ray spectrum observed by *XMM-Newton*. The flux from a heated region on the surface of a NS is modulated with time through the parameter $\alpha(t)$, where $\alpha(t)$ is the time-dependent angle between the pole of the heated region and the observer's line of sight toward the NS. In Figure 3.1 we show the geometry of the heated regions on the surface of RX J0822 4300. We use the notation of Gotthelf et al. (2010), labeling the angle between the rotation axis and the hot spot pole $\zeta$, and labeling the angle between the rotation axis and the observers line of sight $\Psi$. $\alpha_h(t)$ and $\alpha_w(t)$ are the angles between the observer's line of sight and the 'hot' spot and 'warm' spot poles, respectively. We label the corresponding angular radii of the 'hot' spot and the 'warm' spot as $\beta_h$ and $\beta_w$. For fixed viewing angles $\zeta$ and $\Psi$, the values of $\alpha_h(t)$ and $\alpha_w(t)$ will vary sinusoidally:

$$\alpha_h(t) = \arccos[\cos\psi\cos\xi + \sin\psi\sin\xi\cos\gamma_h(t)] \tag{3.1}$$

and

$$\alpha_w(t) = \arccos[\cos\psi\cos\xi + \sin\psi\sin\xi\cos\gamma_w(t)]\,. \tag{3.2}$$

We define two parameters $\delta_\pi$ and $\delta_\gamma$ that specify how the relative positions of the hots spots deviate from a pure antipodal geometry.

$$\alpha_w + \alpha_h = \pi \quad \delta_\pi \tag{3.3}$$

$$\gamma_w = \gamma_h \quad \delta_\gamma \tag{3.4}$$

Adjusting the values of $\delta_\pi$ and $\delta_\gamma$, the warm spot can be placed anywhere on the NS relative to the hot spot. In the special case of an antipodal geometry, $\delta_\pi = 0$ and $\delta_\gamma = 0$. Figure 3.2 shows qualitatively how the energy-dependent pulse modulation and phase are affected by the parameters $\delta_\pi$ and $\delta_\gamma$. In our coordinate system, neither $\delta_\pi$ nor $\delta_\gamma$ can affect the modulation or phase of the hot spot. Changing the value of $\delta_\pi$ can affect the overall spectral modulation only through changing the modulation of the warm spot. Also note that the X-ray pulse phase as a function of energy will always be a step function when $\delta_\gamma = 0$. Evidently $\delta_\gamma \neq 0$ is required to match the observations.

$$\theta(\delta) = \int_0^{R_s/2R} x \, du \Big/ \sqrt{\left(1 \quad \frac{R_s}{R}\right)\left(\frac{R_s}{2R}\right)^2 \quad (1 \quad 2u)u^2x^2} \tag{3.5}$$

where $x \quad \sin\delta$, $R/R_s$ is the NS radius in units of the Schwarzschild radius $R_s = 2GM/c^2$. To improve the efficiency of this calculation we use an approximation presented in Beloborodov (2002):

$$1 \quad \cos\delta = (1 \quad \cos\theta)\left(1 \quad \frac{R_s}{R}\right). \tag{3.6}$$

We adopt a spherical coordinate system where the colatitude angle $\theta$ is measured with respect to the observer's line of sight. Figure 1.2 shows an example photon trajectory for a NS with a typical Schwarzschild radius $R = 2.5\ R_s$. The observed spectrum as a function of rotational phase is computed by integrating over the visible area of the hot spots according to the formula given in Beloborodov (2002):

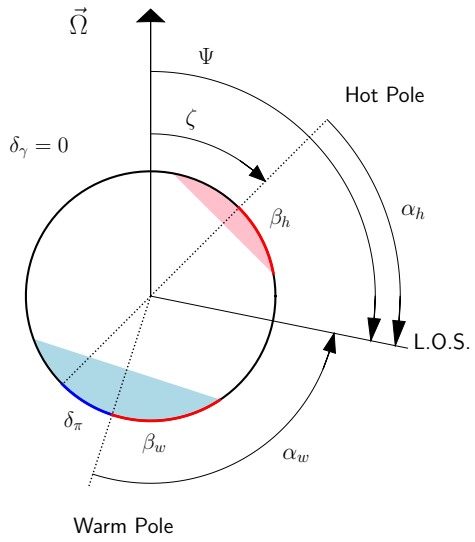


(a) View of the NS with the rotation axis and line of sight (L.O.S.) in the plane of the page. In the geometry shown here the 'phase lag' parameter $\delta_\gamma = 0$, and the phase parameter is set so that equal fractions of both spots are visible. The 'hot' region and 'warm' region are shaded red and blue, respectively.

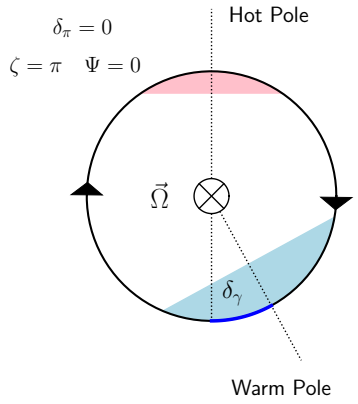


(b) View of the NS with the rotation axis pointing into the page, $\delta_\pi = 0$, and viewing angles set to $\Psi = 0$ and $\zeta = \pi$. In this specific geometry, the hot spot pole and the warm spot pole are in the plane of the page, and 'phase lag' parameter $\delta_\gamma$ is shown.

Figure 3.1: The geometry of the emission model presented in this paper.

$$dF = \left(1 \quad \frac{R_s}{R}\right)^2 I_0(\delta) \cos\delta \frac{dS}{D^2}\,. \tag{3.7}$$

Here $dF$ is the flux from a surface element $dS$, $I_0(\delta)$ is the spectral intensity in the NS rest frame as a function of the emission angle $\delta$, and $D$ is the distance to the NS. We note here that the observed pulse profiles are all consistent with a sinusoid, indicating that the emission is consistent with being isotropic. In the case of isotropic emission, the integration is a simple calculation of the average value of $\cos\delta$ on the NS hot spots.

$$< \cos(\delta) >= \int_{\alpha_h \quad \beta_h}^{min(\alpha_h+\beta_h, \theta_{\max})} d\theta \cos(\delta) \quad \arccos\left[\frac{\cos\beta_h \quad \cos\alpha_h \cos\theta}{\sin\alpha_h \sin\theta}\right] \tag{3.8}$$

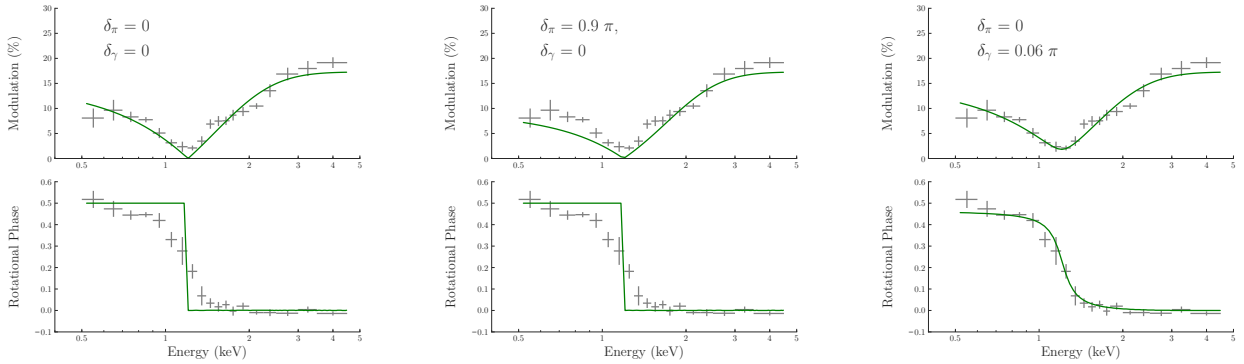


(a) Perfectly antipodal geometry.

(b) Modifying only the $\delta_\pi$ parameter.

(c) Modifying only the $\delta_\gamma$ parameter.

Figure 3.2: Pulse profile modulation and phase as a function of $\delta_\pi$ and $\delta_\gamma$. This plot is only intended to give intuition about how the energy dependent pulse profiles change with these two parameters, and to demonstrate that RX J0822 4300's pulse profiles are inconsistent with an antipodal geometry. Fitting only the modulation and phase of the model to the observed data is not sufficient for accurate modeling, which requires fitting the exact pulse shapes in each energy band, and is done in this paper. Notice that the phase plot will always have a sharp cutoff unless $\delta_\gamma = 0$.

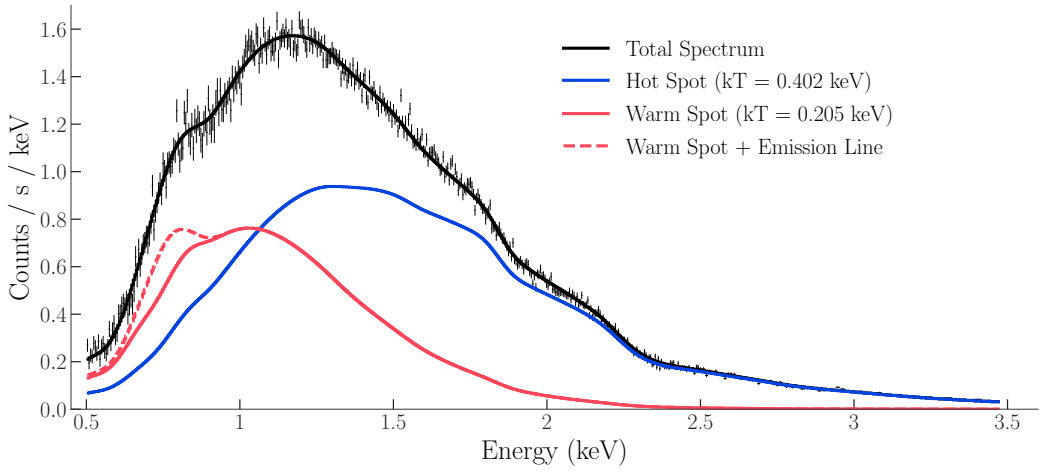


Figure 3.3: The phase averaged spectrum of RX J0822 4300, plotted along with the model. The individual model components from the hot spot, the warm spot and the emission line feature are shown. The redshifted temperatures are indicated in the figure. The temperatures are calculated with high precision by combining the spectral data with the additional constraints required to match the energy-dependent pulse profiles.

where $\theta_{\mathsf{max}}$ is the maximum NS colatitude visible to an observer. When calculating the two dimensional integral of $dF$ over the visible area of a hot spot, there is a trade-off between computational accuracy and speed. It is preferable to take advantage of axial symmetry about the line of sight, and calculate only the one dimensional integral above and use an exact analytic formula for the visible hot spot area if such a formula exists. We use spherical caps to model the hot spots on RX J0822 4300. The area of a spherical cap with angular radius $\beta$ on a NS with radius $R_{NS}$ is $2\pi(1 \quad \cos(\beta))R_{NS}^2$, so this is the value of $\int dS$ when the entire cap is visible. When the spherical cap is only partially visible, we use the exact analytic formula for the area of intersection $I(\theta, r_1, r_2)$ of two spherical caps with angular radii $\mathrm{r}_1$ and $r_2$, separated by an angle $\theta$ on a unit sphere. This is given by equation 1.11 in Chapter 1.

Thus the general formula for the visible area $\int dS$ of a spherical cap with angular radius $\beta$ at colatitude $\alpha$ is

$$\int dS = \begin{cases} 2\pi(1 \quad \cos(\beta))R_{NS}^2 & \alpha + \beta < \theta_{max} \\ I(\pi \quad \alpha, \beta, \theta_{max})R_{NS}^2 & \alpha \quad \beta < \theta_{max} < \alpha + \beta \\ 0 & \alpha \quad \beta > \theta_{max} \end{cases} \tag{3.9}$$

### 3.2.2 Energy-Dependent Pulse Profile Modeling

The amplitudes and phases of energy-dependent pulse profiles are strongly dependent on the temperatures of the two hot spots. This is especially true around the 1.2 keV region where the pulses from the two spots almost perfectly cancel out. The extreme sensitively of the pulse profiles to small changes in the individual hot spot temperatures implies that very accurate measurements of the two hot spot temperatures will result from our modeling. We follow a spectral fitting procedure that uses information from the pulse profiles to measure

the spot temperatures much more accurately than what can be achieved through spectral modeling alone. We search through different temperatures of the 'warm' and 'hot' spots by holding the 'warm' spot temperature fixed and allowing the rest of the model parameters to vary to fit the phase-averaged spectrum. We repeated this for a range of values of the warm spot, and for each set of warm spot/hot spot temperature pairs consistent with the phase-averaged spectra, we fold the absorbed spectrum of each spot through the *XMM-Newton* detector response matrix and compute the phase averaged in each of 16 energy bands. Each energy band is divided into 18 phase bins. We identify the pair of temperatures that are best able to reproduce the energy-dependent pulse profiles as the correct, redshifted temperatures. We find that the values of the 'warm' spot and 'hot' spot most consistent with the energy-dependent pulse profiles are 0.205 keV and 0.402 keV, respectively. The parameters of this phase-averaged spectral model are listed in Table 3.3, and the phase-averaged spectrum is shown in Figure 3.3.

We have now calculated the correct hot spot temperatures (as seen by an observer at infinity), as well as the intrinsic pulsation amplitudes and relative phase of the two spectral components. We can now determine the corresponding values of the viewing angles $\zeta$ and $\Psi$, and also the position of the 'warm' spot relative to the 'hot' spot parameterized by the angles $\delta_\pi$ and $\delta_\gamma$. We compute the time-dependent spectra from our general relativistic emission model over the four-dimensional parameter space of all plausible combinations of the physical parameters $\zeta$, $\Psi$, $\delta_\pi$ and $\delta_\gamma$. In order to compute these spectra it is necessary to know the values of the hot spot sizes $\beta_w$ and $\beta_h$ for all of the possible values of $\zeta$, $\Psi$, $\delta_\pi$ and $\delta_\gamma$. Figure 3.4 shows some examples of these 'beta maps', i.e. maps of the sizes of the hot and warm spot as a function of the observers viewing angle $\zeta$ and $\Psi$. We note that there is only one beta map for the 'hot' spot, since its position relative to the observer is the same for all values of $\delta_\pi$ and $\delta_\gamma$. For the warm spot we construct 'beta maps' for all combinations

of the parameters $\delta_\pi$ and $\delta_\gamma$.

Now for each pair of these four parameters we know the corresponding hot spot sizes, and we compute the values of the two pulsation amplitudes and the relative phase from our emission model. Using this mapping between the physical parameters of the NS geometry and the two pulsation amplitudes and the relative phase of the two spectral components, we calculate the pulse profiles corresponding to each set of physical parameters. We then record the chi-square values obtained from comparing each set of theoretical energy-dependent pulse profiles to the data. We derive constraints on $\zeta$, $\Psi$, $\delta_\pi$ and $\delta_\gamma$ by calculating the magnitude of the chi-square deviations above the best fit value. The best model parameters for a 1.4 M NS at the estimated distance of 1.3 kpc are listed in Table 3.4, and the best fit theoretical pulse profiles are plotted with the data in Figure 3.6. Chi-square plots around the best fit values of $\zeta$, $\Psi$, $\delta_\pi$ and $\delta_\gamma$ are shown in Figure 3.7a and 3.7b.

| Parameter | Value |
|---|---|
| $N_{\mathsf{H}}$ | 0.73 $10^{22}$ cm $^{2}$ |
| $kT_{\mathsf{warm}}$ | 0.205 keV |
| $L_{\mathsf{warm}}$ | 1.5 $10^{34}$ $D^2_{1.3}$ erg s $^{1}$ |
| $kT_{\mathsf{hot}}$ | 0.402 keV |
| $L_{\mathsf{hot}}$ | 1.0 $10^{34}$ $D^2_{1.3}$ erg s $^{1}$ |
| $E_{\mathsf{line}}$ | 0.75 keV |
| $\sigma_{\mathsf{line}}$ | 0.05 keV |
| $F_{\mathsf{line}}$ | 5.6 10 $^{4}$ photons cm $^{2}$ s $^{1}$ |

Table 3.3: Observed spectral parameters of RX J0822 4300. $D_{1.3}$ is the distance in units of 1.3 kpc. The energies of the two blackbodies and the emission line are the redshifted values. The blackbody luminosities are the unabsorbed values.

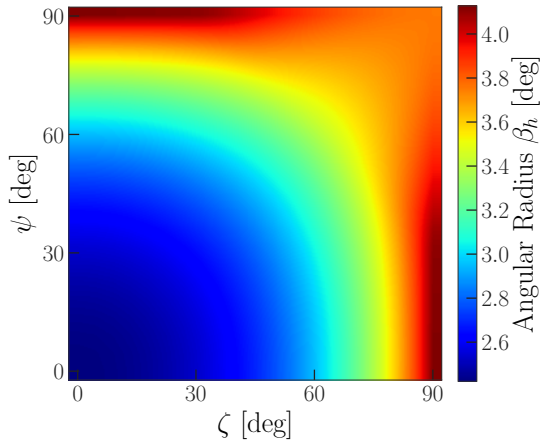


(a) Hot spot size as a function of the viewing angles.

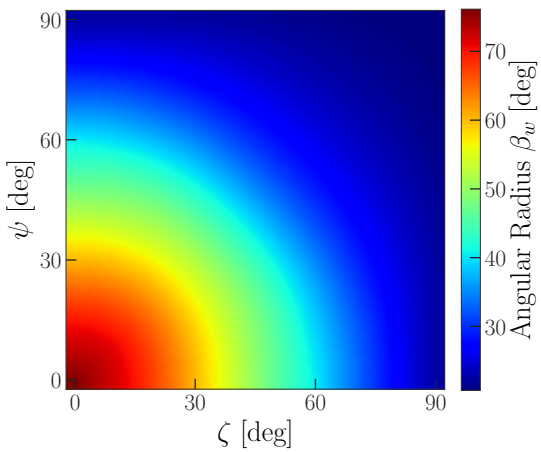


(b) Warm spot size with $\delta_\pi = 0$.

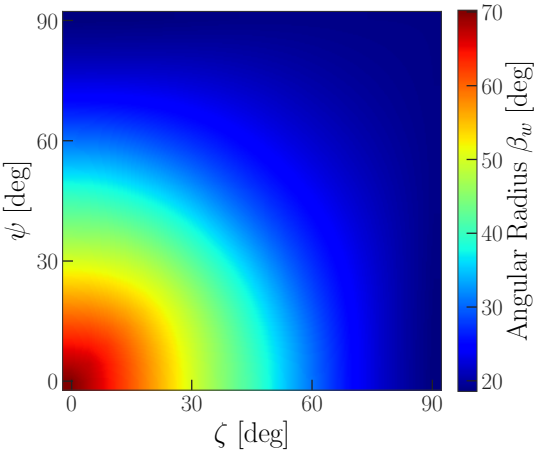


(c) Warm spot size with $\delta_\pi = 0.25\ \pi$.

Figure 3.4: The sizes of the heated regions as a function of viewing angles, $\psi$ and $\zeta$, and their relative positions, parameterized by the angles $\delta_\pi$ and $\delta_\gamma$. In our adopted coordinate system the hot spot size is independent of $\delta_\pi$ and $\delta_\gamma$. The warm spot size is a function of $\delta_\pi$ and it is independent of $\delta_\gamma$. Two representative beta maps for the warm heated region are shown above. The warm spot angular radius tends to decrease as $\delta_\pi$ increases. This is because larger values of $\delta_\pi$ correspond to smaller rotation-averaged colatitudes of the warm spot.

| Parameter | Value | Description |
|---|---|---|
| $\beta_h$ | 4 degrees | Hot spot angular size |
| $\beta_w$ | 24 degrees | Warm spot angular size |
| $\delta_\pi$ | 17 degrees | First dipole offset angle |
| $\delta_\gamma$ | 0.04 rotation cycles | Second dipole offset angle |
| $\zeta$ | 6 degrees | Angle between hot spot pole and rotation axis |
| $\Psi$ | 83 degrees | Angle between the line of sight and rotation axis |
| $R_{NS}$ | 12 km | Assumed Neutron Star Radius |
| $D$ | 1.3 kpc | Assumed Neutron Star Distance |
| $kT_{\mathsf{hot}}$ | 0.402 keV | Hot spot temperature |
| $kT_{\mathsf{warm}}$ | 0.205 keV | Warm spot temperature |

Table 3.4: Best fit model parameters for a 1.4 M , 12 km radius neutron star. The model is symmetric with respect to the interchange of the angles $\zeta$ and $\Psi$.

### 3.2.3 Insensitivity of Results to Values of the Neutron Star Radius and Distance

Up to this point, we have modeled RX J0822 4300 as a 12 km radius, 1.4 M neutron star at a distance of 1.3 kpc. It turns out, owing to the particular viewing geometry toward RX J0822 4300 and the relatively small size of its hot spots, that the values of $\zeta$, $\Psi$, $\delta_\gamma$ and $\delta_\pi$ are very insensitive to different distance and radius estimates. Figure 3.5 shows how the spot sizes and pulsed fractions change as a function of distance and radius, with all other model parameters held fixed. For each distance and NS radius value pair, we calculate the required spot sizes necessary to match the observed flux, and hence the pulsation amplitude with these new distance and radius parameters. In the region of our model parameter space where we can change the distance and spot sizes without effecting pulsation amplitudes, we can be confident that the other model parameters are independent of the distance estimate. In particular, we find that for any distance in the range of 1.0 1.6 kpc, both hot spots are

small enough that their pulsation amplitudes change by negligible magnitudes with distance, and therefore the values of $\zeta$, $\Psi$, $\delta_\gamma$ and $\delta_\pi$ are invariant with respect to distance. We note that while it is possible to change the NS distance and keep all other model parameters fixed (except for the spot sizes), changing the NS radius and keeping all other parameters fixed except for the spot sizes will necessarily modify the spot pulsation amplitudes.

### 3.2.4 Most Probable Magnetic Inclination Angle

Following Gotthelf et al. (2010), we can calculate the most probable magnetic inclination angle, even though our model is symmetric with respect to the interchange of $\Psi$ and $\zeta$. Since $\Psi$, the angle between the rotation axis and the observer's line of sight, is random, it should be a sinusoidally distributed random variable. This means that the relative probability of $\Psi$ being the angle between the rotation axis and the line of sight is equal to $\sin(\Psi)/\sin(\zeta)$ 10. There is a $> 90\%$ probability that we are viewing the neutron star with its rotation axis almost perpendicular to our line of sight.

## 3.3 Discussion

The exquisite resolution of the X-ray data of RX J0822 4300 has allowed to map the temperature profile on the surface of the star, in addition to constraining its viewing geometry. The current data have confirmed the presence of two antipodal spots, as already found by (Gotthelf et al. 2010), but they have also uncovered the presence of an offset of about 17 deg with respect to the (perfectly) antipodal configuration identified in the previous, lower-resolution study.

The most natural explanation for temperature anisotropies on the surface of NSs can be ascribed to the effect of crustal magnetic fields, which leave their imprint on the surface

temperature distribution of the NS, and hence on its pulsed X-ray emission (Greenstein & Hartke 1983; Goldreich & Reisenegger 1992; Page 1995; Heyl & Hernquist 1998; Potekhin & Yakovlev 2001; Lai 2001; Hollerbach & Rüdiger 2002; Geppert et al. 2004; Cumming et al. 2004; Geppert et al. 2006; Pérez-Azorín et al. 2006; Zane & Turolla 2006; Pons et al. 2009; Gonzalez & Reisenegger 2010; Perna & Pons 2011; Glampedakis et al. 2011; Pons & Perna 2011; Viganò et al. 2013; Perna et al. 2013; Geppert & Viganò 2014; Gourgouliatos & Hollerbach 2018). The degree of temperature anisotropy is controlled by the ratio between the thermal conductivity along and across the field lines: In the outer 100 m of a NS, the temperature gradient in the radial direction is very high, and heat is efficiently transported along the radial direction, thermally connecting the surface to the inner crust and the core. On the other hand, crustal regions where the $B$-field is nearly tangential are thermally insulated and not connected to the hot core, hence remaining cooler.

As the star ages, the magnetic field and the temperature evolve in a coupled fashion. The Lorentz force in the induction equation causes the Hall drift of the field lines, while the Joule term is responsible for Ohmic dissipation, which affects the temperature. The time-dependent temperature/magnetic field structure at a given age depends both on the macrophysics of the star, as well as on the initial magnetic field configuration. For a magnetic field which is predominantly poloidal at birth, the temperature profile is symmetric with respect to the equator, and the symmetry is maintained throughout the evolution. However, the presence of strong internal toroidal components can radically change this topology. If the toroidal field is dipolar, i.e aligned with the poloidal field, the equatorial symmetry is broken due to the Hall drift during the evolution (see i.e. Hollerbach & Rüdiger 2002; Viganò et al. 2013), and it results in a complex field geometry with asymmetric north and south hemispheres (Geppert et al. 2006; Perna et al. 2013; Geppert & Viganò 2014). The region with tangential field lines does not coincide with the equator, resulting in asymmetric

temperature profiles. The degree of anisotropy strongly depends on the initial toroidal field strength because of its insulating effect in the crust. Magnetothermal simulations (i.e. Geppert et al. 2004; Perna et al. 2013; Geppert & Viganò 2014) have showed that temperature differences by more than a factor of two between the two hemispheres can be produced in older, evolved objects. Note that magnetothermal simulations to date have been largely 2D (axial symmetry) for computational reasons; hence the initial field configurations have azimuthal symmetry, and so does the resulting temperature profile. Magnetothermal simulations in 3D have recently begun (Gourgouliatos & Hollerbach 2018) and shown that, in models in which the dipolar field is misaligned with the toroidal field, the location of the hot spots is no longer aligned with the axis of the dipolar field, since the formation of the hot spots is very sensitive to the toroidal field.

Based on the discussion above, it is apparent that, at least at a qualitative level, a surface temperature distribution of the kind inferred in RX J0822 4300 is plausible in NSs. However, there is an important caveat in the direct application to RX J0822 4300, and that is the fact that strong temperature anisotropies require relatively large magnetic fields. An investigation by Geppert & Viganò (2014) into the formation of (magnetically-generated) hot spots identified a number of important conditions for the formation of such spots, including a minimum dipolar field strength $B_{\mathsf{dip}}$ & 5 $10^{12}$ G and a maximum toroidal field in the crust, $B_{\mathsf{tor}}$ . $10^{15}$ G. While the latter is hidden in the crust and mainly revealed through its effects on the surface temperature, the former is also independently measured from the spin-down rate. In the case of RX J0822 4300, the field inferred from the spin down rate is $B_s = 2.9$ $10^{10}$ G, which is in apparent tension with the above results taken at face value. Possible ways to ameliorate this tension may require RX J0822 4300 to have a poloidal field with stronger-than-dipolar multipoles and/or the presence of material (such as a fallback disk left over from the supernova explosion) which provides additional torque to the star,

and may hence affect the field measurement from spin down alone (see i.e. Yan et al. 2012).

Alternatively, the temperature anisotropy observed in RX J0822 4300(as well as its timing properties) could be interpreted within the context of a 'buried' field scenario (Geppert et al. 1999; Ho 2011; Shabaltas & Lai 2012; Viganò & Pons 2012). The NS does not need to be born with a very low magnetic field, like in the 'antimagnetar' scenario, but it could have a typical field which is buried by an episode of hypercritical accretion following the supernova explosion. This leads to an external magnetic field (responsible for the spin down of the star) much lower than the internal 'hidden' $B$ field. This model has the distinctive feature of producing hot polar caps since the buried $B$ field keeps the equatorial surface regions insulated from the hot core (Viganò & Pons 2012). The additional advantage of this model is that, unlike in the standard magnetothermal evolution where hot spots form on a timescales of at least 10 kyr, in this scenario the hot regions form on a much shorter timescale, as low as kyr, hence more compatible with the young age of 3.7 kyr inferred for RX J0822 4300.

It is interesting to compare RX J0822 4300 to PSR J1852+0040 the CCO in the Kes79 supernova remnant. Bogdanov (2014) used a similar general relativistic modeling technique to model the pulsations from PSR J1852+0040 that are, unlike RX J0822 4300, strongly pulsed and significantly broader than a pure sinusoid. This indicates that either the emission is strongly beamed, or alternatively that the heated surface region has a very extended, non-circular shape. The magnetic inclination angle of the CCO in Kes 79 is uncertain, despite its large pulsed fraction, because the radiation pattern is degenerate with respect to the inclination angle (Bogdanov 2014). The only other CCO with detected X-ray pulsations is 1E 1207.4 5209. 1E 1207.4 5209 has a small pulsed fraction of 10%. There is no evidence of an energy dependent phase reversal in the pulse profiles of 1E 1207.4 5209. Evidently the two-temperature spectral components are approximately co-located on the stellar surface.

Because 1E 1207.4  5209 only has one surface thermal region producing its observed pulse profile, we can conclude that it must have a relatively small ($< 15$  angular radius) magnetic inclination angle.

A small (or undetectable) pulsation level is common to all the CCOs (with the exception of the CCO in Kes 79), and hence something potentially interesting as a diagnostic of their nature Gotthelf et al. (2013). In the case of Puppis A, it is likely the result of a small inclination angle between the emitting regions and the rotation axis. In the buried field scenario, the re-emergence of the field occurs on a timescale  $10^3$  $10^5$ kyr. Simulations by Viganò & Pons (2012) for a representative case with an internal toroidal field of $10^{15}$ G, and a partially re-emerged dipolar field of $10^{10}$ G show that, at an age of a few kyr and for a crustal-confined magnetic field model, the star displays hot polar caps. Hence, in this scenario, the hot regions correspond to the axis of the dipolar field. The small inclination axis between the dipolar and rotation axis can then be interpreted within the evolutionary model of Dall'Osso & Perna (2017), which couples interior NS viscosity and magnetic field evolution to predict the expected range of tilt angles of young neutron stars. At the period of 112 ms, a small inclination angle is predicted for NSs with magnetically induced ellipticities $\epsilon_B$ & a few  $10^{-7}$, with the specific value dependent on the mass and radius of the NS. Hence a large internal field in the hidden field scenario can explain both the observed anisotropic temperature distribution, as well as the small observed tilt angle.

## 3.4 Summary

CCOs are an interesting class of NSs suspected to have internal magnetic fields much stronger than their external (dipolar) ones. Here we have reported the results of the analysis of 470 ks of *XMM-Newton* observations of a special member of this class, that is the CCO in

the Puppis A supernova remnant. The large wealth of exquisite data allowed us to perform a detailed analysis of the energy-dependent pulse profile in sixteen energy bands. Our modeling, which accounts for the general relativistic effects of light bending and gravitational redshift, allowed us to map the temperature distribution on the star surface, in addition to constraining the viewing/emission geometry.

We uncovered an asymmetric temperature distribution, with one large warm region with a 24 degree angular radius, and a second, hotter one with a 4 degree angular radius (for the best estimated distance of 1.3 kpc), with the warm spot offset from an antipodal configuration by 17 degrees. We hence discussed the production of such a small hot spot within the context of the 'antimagnetar' scenario or, alternatively, as arising within a 'buried field' scenario.

# Appendix: *XMM-Newton* pn Detector Background Subtraction

When the *XMM-Newton* pn detector is operated in small window mode, the entire CCD, not just the small window, is illuminated. In this configuration there are out-of-time events from the CCD region outside of the small window. Since the CCD region outside the small window sometimes detects photons from the Puppis A supernova remnant, the background count rate is roll angle dependent. The *XMM-Newton* roll angle is a function of the position of *XMM-Newton* relative to the Sun, and the higher background count rate affects the observations performed in the months of April and May. This may mean that the standard background subtraction is imperfect.

We tested for the possibility of imperfect background subtraction by experimenting with different background scaling factors. We implemented this background scaling using the HEASoft tool `grppha`. The background scaling factor was stepped through values of 0.80 to

1.20 in steps of 0.01. All datasets were combined into one spectrum with the HEASoft tool `addascaspec`. We also divided the datasets into two groups with high and low roll angles, and combined the spectra in these two separate groups. These three combined spectra, as well as each individual spectrum, were fitted with simple two blackbody models, i.e. without an emission or absorption line feature, and the chi-square values were calculated for each value of the background scaling factor. We found that, in all cases, the fit to the spectrum is worse with the pure two blackbody model than when the model includes an emission line feature. If the emission feature was due to contamination from the SNR, our variable background scaling procedure would have allowed us to achieve a better fit to a pure blackbody spectrum for some value of the background scaling factor. Because the inclusion of the line results in better fits to the source spectrum in all cases, we conclude the emission line feature is intrinsic to the source spectrum.

Next, simultaneously fitting a two blackbody plus gaussian emission line model to all nineteen observations, we looked for variability in the emission feature. The column density of interstellar absorbing material and the gaussian line width were held constant across all observations, and the other parameters were allowed to vary independently. The photo-electric absorption by the interstellar medium was modeled with the Tuebingen-Boulder ISM absorption model, implemented as `tbabs` in `Xspec`. For each observation, the residuals of the fit of the models to the data were small and showed no need for any additional model components. The central energy of the gaussian line is around 0.75 keV. We find that the emission line central energy, width and normalization are, to within statistical uncertainties, invariant between observations. In particular we found no significant difference in the source spectra of the observations with different background rates. In summary, the inclusion of the emission line feature results in optimal fits to each dataset, regardless of background rates, and it can be modeled as a time-invariant to within statistical uncertainties of the data.

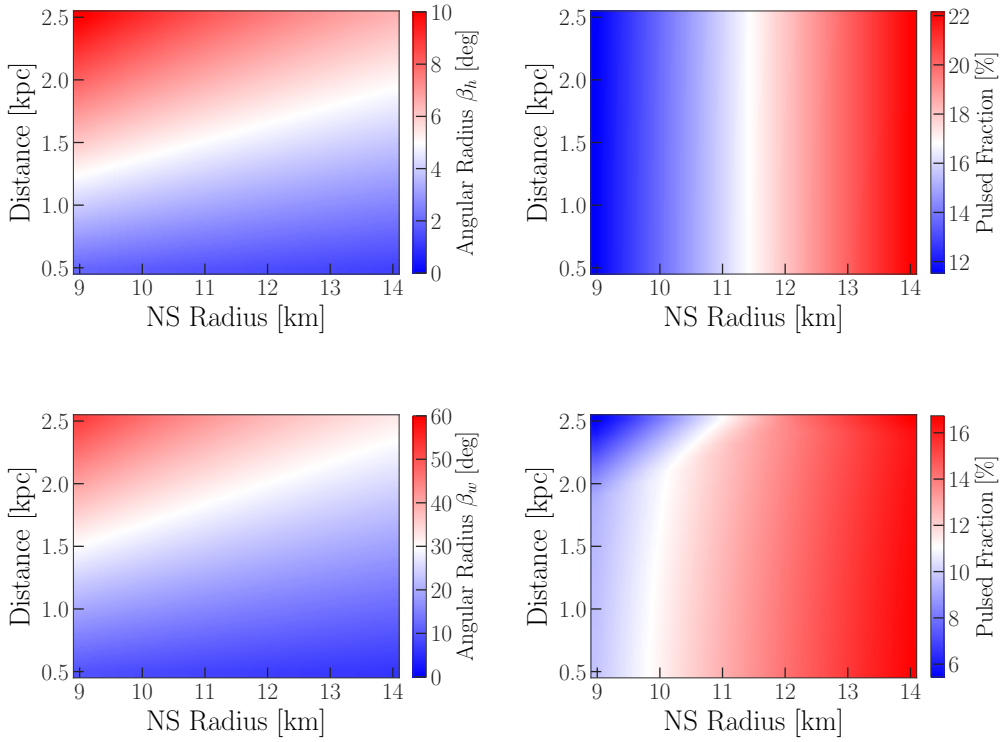


Figure 3.5: We explore the sensitivity of our model to changes in the NS radius and distance parameters. The angles $\zeta$ and $\psi$ are fixed at 83 and 6 degrees, respectively. **Top left**: Size of the hot spot for a range of values of the NS radius and distance. In order to match the observed flux, the spot angular size must increase as a function of distance and decrease as a function of NS radius. **Top right**: Pulsed fraction as a function of distance and NS radius, computed using the corresponding $\beta_h$ values from the plot on the left. Note that the pulsed fraction has almost no dependence on the distance to RX J0822 4300 even though the hot spot angular radius changes by as much as a factor of five. The implication is that our measured values for the parameters $\zeta, \psi, \delta_\pi$ and $\delta_\gamma$ are very robust, despite the only approximately known distance to Puppis A. **Bottom left**: Size of the warm spot for a range of values of the NS radius and distance. **Bottom right**: Pulsed fraction as a function of distance and NS radius, computed using the corresponding $\beta_w$ values from the plot on the left. The warm spot is larger and its pulsed fraction does vary with distance especially at for small values of the NS radius. We note however that within the 1.0 1.6 kpc distance range expected for RX J0822 4300 the pulsed fraction is almost invariant with respect to distances changes. We can conclude that the results of our modeling are distance independent for any reasonable NS radius and any distance with the expected range of 1.0 1.6 kpc.

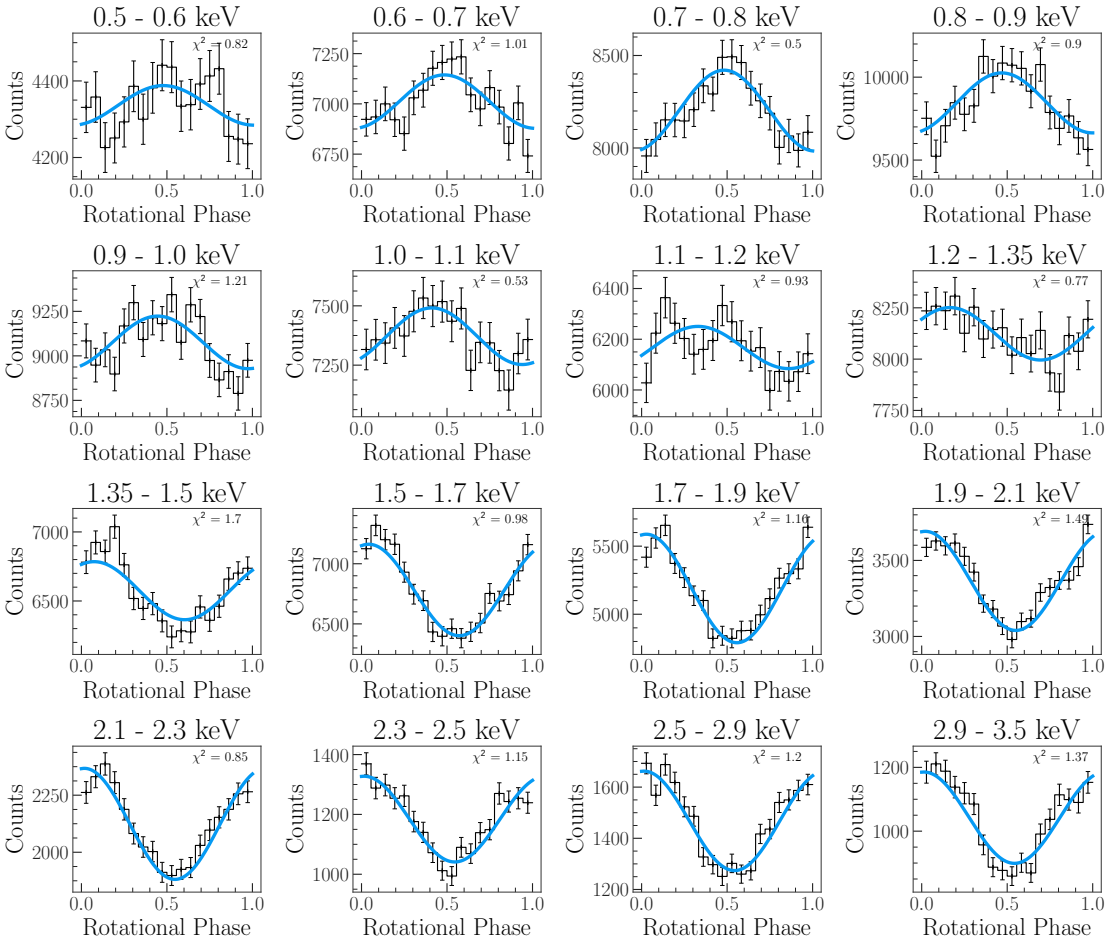


Figure 3.6: Energy dependent pulse profiles are plotted along with the theoretical model in 16 energy bands. The background counts are included in each band and also in the theoretical model. The $\chi^2$ value for each individual energy band is indicated inside each subplot.

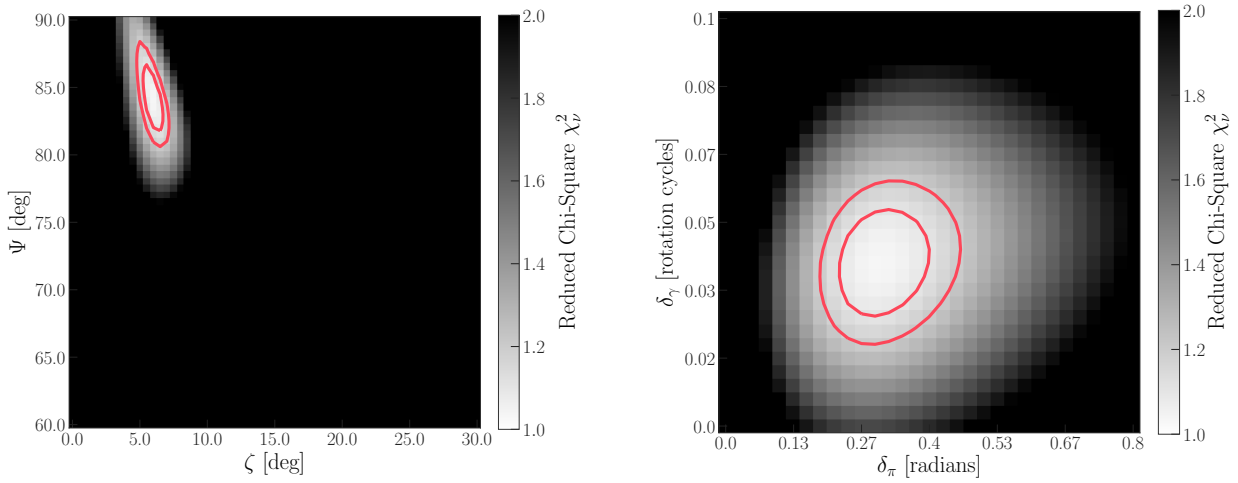


(a) Chi square contours for the viewing angles $\Psi$ and $\zeta$ The offset angles were held fixed at $\delta_\pi = 0.3$ rad and $\delta_\gamma = 0.04$ cycles. Note that the emission model is symmetric with respect to interchanging $\Psi$ and $\zeta$. The 90 percent and 99 percent confidence regions are indicated by the red contours.

(b) Chi square contours for the warm spot offset angles. $\delta_\gamma$ and $\delta_\pi$ uniquely determine the position of the warm spot relative to the hot spot, with $\delta_\gamma = \delta_\pi = 0$ corresponding to the perfectly antipodal configuration. The viewing angles were held fixed at their best fit values of 83 and 6 degrees. The 90 percent and 99 percent confidence regions are indicated by the red contours.

Figure 3.7: Results of the search over the 4 dimensional parameter space of the two viewing angle $\zeta$ and $\Psi$, and the two dipole offset angles, $\delta_\gamma$ and $\delta_\pi$

.

# Chapter 4

# Modelling the Post-Outburst State of XTE J1810-197

## 4.1 The Transient Magnetar XTE J1810 197

XTE J1810 197 is the canonical example of a transient magnetar. Since Ibrahim et al. (2004) reported on its 2003 outburst observed with the Rossi X-ray Timing Explorer, XTE J1810 197 has transformed our understanding of the physics of magnetars. We now know of 10 transient magnetars (depending on how one chooses to define them, and classify candidate sources), objects whose outbursts and subsequent flux decays are similar to XTE J1810 197. Halpern et al. (2005) reported the first observations of radio emission from a magnetar, a previously unexpected phenomenon. The radio emission from XTE J1810 197 was observed only during the early years of its outburst, and disappeared in late 2008 (Camilo et al. 2006, 2016). We now know of four other transient magnetars that produce pulsed radio emission during their X-ray outbursts: the magnetar in the galactic center SGR J1745 2900, 1E 1547.0 5408, PSR J1622 4950, and most recently Swift J1818.0 1607

(Shannon & Johnston 2013; Camilo et al. 2007; Levin et al. 2010; Esposito et al. 2020).

The flux from XTE J1810  197 decreased exponentially after its 2003 outburst, from a bolometric luminosity of 2  $10^{35}$ erg/s in September 2003 to 4  $10^{34}$ erg/s when it reached a steady state in 2009. Its spectrum at the beginning of the 2003 outburst was dominated by flux from a hot region covering  30% of the NS surface, well described by a two blackbody model with initial temperatures of  0.7 keV and  0.25 keV. The hot spot shrank and cooled over continuously until reaching a size of about 1% of the surface area of XTE J1810  197 and a temperature of  0.3 keV. This behaviour of shrinking and cooling hot spots on transient magnetars is explained by the untwisting magnetosphere model Beloborodov (2009). The steady state spectrum had a constant flux, temperature and remarkably steady spin-down rate Alford & Halpern (2016); Camilo et al. (2016).

Alford & Halpern (2016) reported on the long-term evolution of the X-ray properties of XTE J1810  197 from its 2003 outburst through 2014. The most interesting result of that analysis was that XTE J1810  197's hot spot continues to emit X-rays at a luminosity exceeding the luminosity that can be explained by rotational energy loss (6.6  $10^{32}$ erg/s). The conclusion is that XTE J1810  197's luminosity continues to be powered by magnetic field decay. This long persistence of the hot emitting regions was not expected, and therefore has the potential to further inform magnetar theory.

The viewing and emission geometry of XTE J1810  197 has previously been modeled by Perna & Gotthelf (2008) and Bernardini et al. (2011). Both of these analyses included the import effects of light bending and gravitational redshift to calculate the hot spot sizes and the viewing angle geometry of XTE J1810  197. Perna & Gotthelf (2008) used a two blackbody model to model the X-ray emission from XTE J1810  197's heated surface during the beginning of the outburst from September 2003 to March 2006. This model accurately reproduced the first two years of observations where the pulsed fraction as a function of

energy rises from  20% at energies less than 0.5 keV to  40% at energies greater than 2 keV. However this model could not reproduce the energy dependent pulse profiles in the 2005 and 2006 observation, when the hot spot flux had significantly decreased. They speculated that this was because of the need to include unpulsed emission from the whole surface of the star in their model, in order to suppress the pulsed fractions at lower energies. Bernardini et al. (2011) modeled the emission from XTE J1810  197 just as it reached a quiescent state in September 2009. They included emission from the whole surface of the magnetar, but found that they could only reproduce the observed energy dependent pulse profiles by assuming that the emission from the hot spot is anisotropic and strongly beamed in the radial direction. Even with anisotropic emission, the model was not a perfect fit to both the phase-averaged spectrum and pulse profiles. In this analysis we will attempt to model the X-ray pulsations from XTE J1810  197 with a model that is a better fit to the X-ray spectrum and pulse profile, while also allowing for a smaller, more physical NS radius.. We will find that the only way to reproduce the pulse profiles of XTE J1810  197 is by using a model with a NS mass of 1.9M , larger than the canonical 1.4 M  neutron star.

## 4.2 Modeling the Post-Outburst Steady State of XTE J1810-197

Table 4.2 shows the six *XMM-Newton* observations that were combined for this analysis. The data were reduced and extracted using the Science Analysis Software version 13.5. We only used data from the EPIC pn CCD because of its long term stability and throughput at low energies. All observations were performed in Imaging Large Window mode. The data were filtered to remove time intervals with high-energy flares, and events with FLAG = 0 and PATTERN  4 were selected from these good time intervals. Circular source and

Table 4.1: Log of *XMM-Newton* Observations

| ObsID | Date (UT) | Exposure (ks) | Net Counts (0.3 - 10 keV) |
|---|---|---|---|
| 0671060101 | 2011 Apr 3 | 22.9 | 6975 |
| 0671060201 | 2011 Sep 9 | 15.9 | 5206 |
| 0691070301 | 2012 Sep 6 | 17.9 | 6335 |
| 0691070401 | 2013 Mar 3 | 17.9 | 3170 |
| 0720780201 | 2013 Sep 5 | 24.5 | 7857 |
| 0720780301 | 2014 Mar 4 | 26.0 | 8200 |

Table 4.2: *XMM-Newton* observations of XTE J1810  197 during its post-outburst steady state. All spectra and pulse profile were combined for this analysis.

background regions were created with radii of $45^{00}$, or sometimes as small as $30^{00}$ in order to avoid overlap with the edge of a detector chip. The pulse profiles from each observation were combined by fitting them to a sine curve and shifting the phases into alignment. We note that the fact the pulse profiles are well described by a sinusoidal model is evidence that the emission from XTE J1810  197 is isotropic. Strongly anisotropic emission, which is observed in other magnetars and was observed at beginning of XTE J1810  197's 2003 outburst, tends to produce non-sinusoidal pulse shapes.

We follow a procedure very similar to the process used to fit the pulse profiles of RX J0822  4300 described in Chapter 3. All of the equations for hot spot fluxes, light bending, etc. are the same, with the simplification that now we have only one hot spot to model on a NS surface which has a constant flux. We first fit the spectrum of XTE J1810  197 to an empirical two blackbody model and calculate the best fit temperature and flux normalizations. This spectrum and empirical two blackbody model is shown in Figure 3.3. The blackbody temperatures in the observers frame are 0.15 keV and 0.26 keV and the absorbing column density is 0.94 cm  $^{2}$. We model XTE J1810  197 using a distance of 3 kpc, a NS radius of 13 km, and a mass of 1.9 M  , and calculate the hot spot size as a function of the viewing

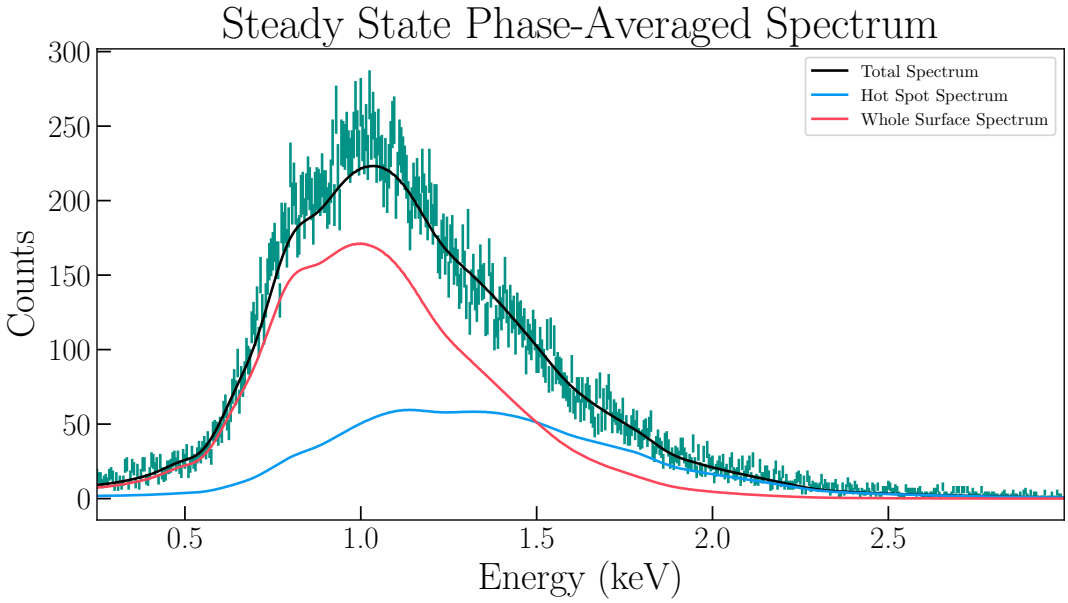


Figure 4.1: Phase-averaged spectrum of XTE J1810  197 and the two-blackbody model with individual components shown.

angles $\Psi$ and the magnetic inclination angle $\zeta$. This 'beta map', the angular radius of the hot spot as function of all possible viewing geometries is shown in Figure 4.2.

For each pair of $\Psi$ and $\zeta$, we use our general relativistic light bending code to produce theoretical pulse profiles in four energy bands. We compare these theoretical pulse profiles to the data in four energy bands and produce a chi-square plot of the most probable values of $\Psi$ and $\zeta$ in Figure 4.3. In Figure 4.4, we plot the best fit theoretical pulse profiles (with $\Psi = \zeta = 53$ ), and the observed pulse profiles in four energy bands. We are able to reproduce the observed increasing pulse fraction accurately.

We are able to reproduce the observed increasing pulse fraction as a function of energy. This increase is observed because of the presence of the lower temperature spectrum of the whole surface suppressing the pulsations at low energies. Previous studies required a anisotropic emission in order to reproduce this effect, but it seems to be unnecessary.

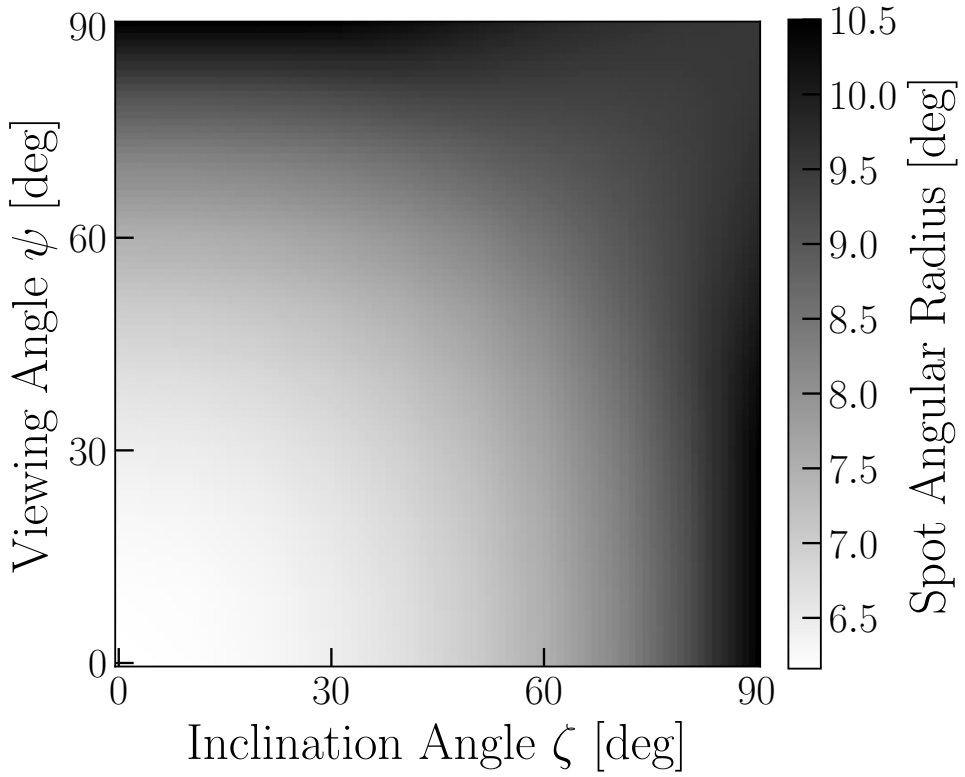


Figure 4.2: Size of the hot spot on the surface of XTE J1810 197 as a function of $\Psi$ and $\zeta$.

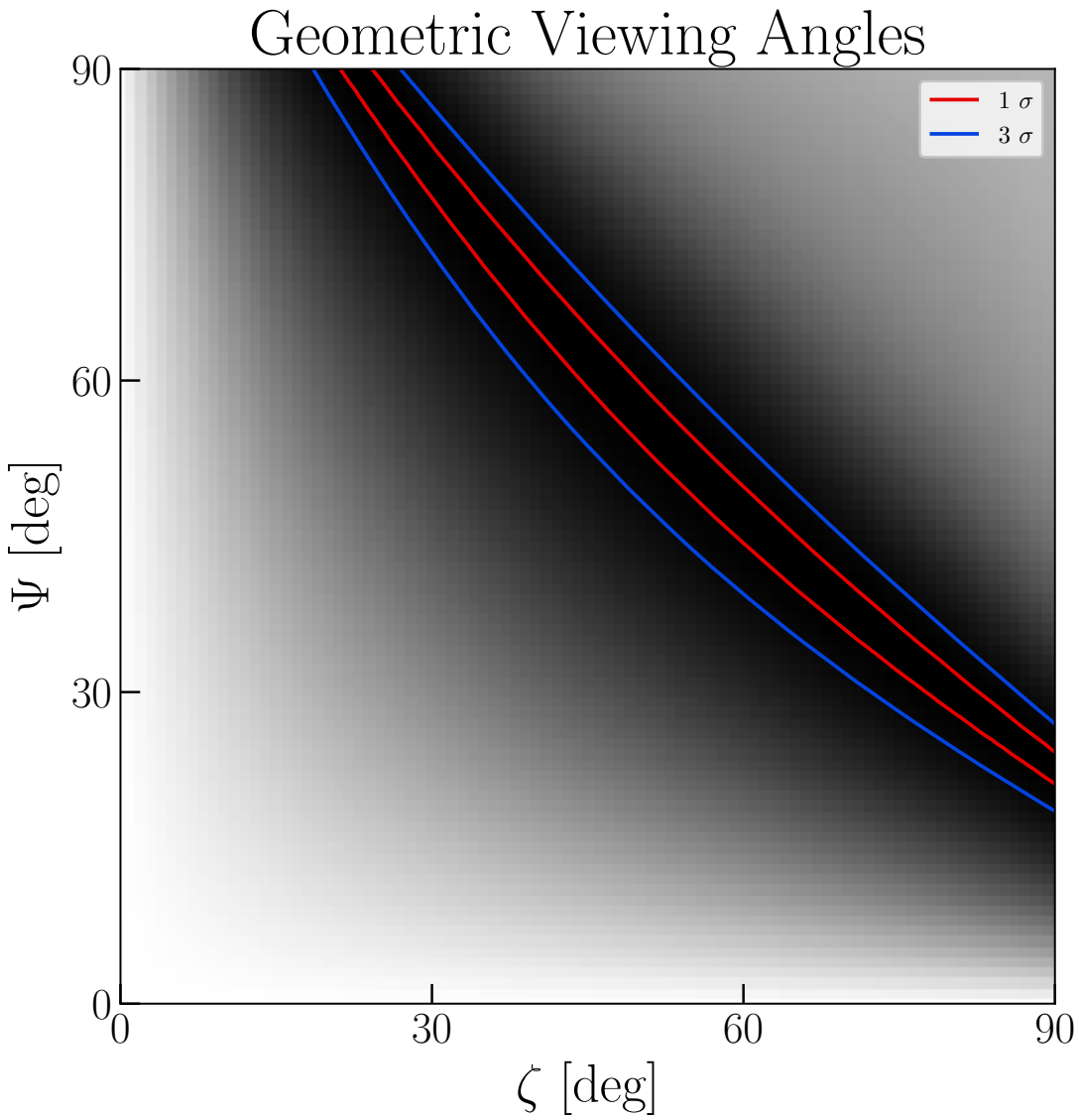


Figure 4.3: Chi-square contours of the most probable viewing angles describing the position of the hot spot on XTE J1810 197. The chi-square statistics were calculated by comparing the modelled pulse profiles to the *XMM-Newton* data in each energy band.

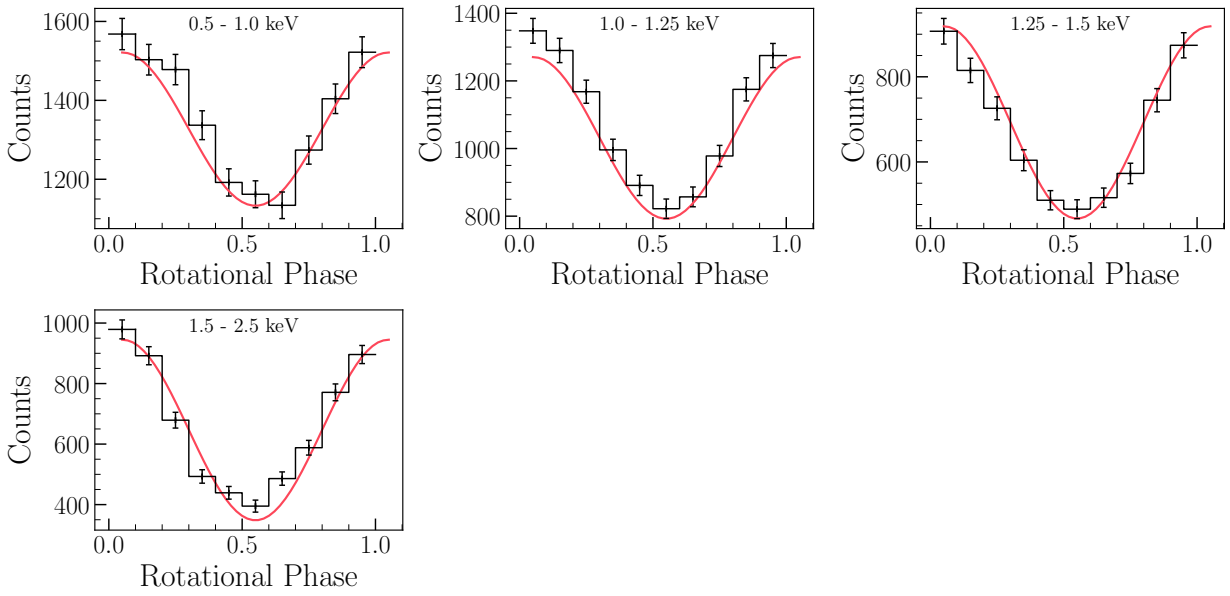


Figure 4.4: Observed energy dependent pulse profiles and pulse profiles computed with the theoretical model. Note that the modulation increases as a function of energy. Unlike previous studies, we find that anisotropic emission is not required, and we can naturally account for the increasing modulation with energy caused by the 'whole surface' spectral component suppressing the pulsations at low energies. This is because we modeling the emission from the 'whole surface' of XTE J1810  197 using a model with a larger NS mass, thus allowing us to achieve both a better fit to the X-ray spectrum and also a better fit to the observed pulse profiles. In this model $\Psi = \zeta = 53$ .

## 4.3 Evidence Suggestive of a Massive Magnetar

The interpretation of the soft X-ray component of the spectrum XTE J1810  197 in its quiescent state has been difficult. Observations of XTE J1810  197 in the first few years after its 2003 outburst did not even include this component since it was not statistically significant when the flux from the large hot spot dominated the spectrum. Bernardini et al. (2009) recognized that a softer component was indeed present a few years post outburst, and that its surface area was so large it was likely emission from the whole surface of the magnetar. Even before this, there were hints that a whole surface emission component would be necessary in the modeling results of Perna & Gotthelf (2008). Alford & Halpern (2016) noticed that the NS radius implied by this spectral component was too large, and suggested that a large mass was likely. Having done more detailed general relativistic modeling of XTE J1810  197, we now believe that this is indeed that case.

In Figure 4.5, we plot the radius of the soft X-ray component of XTE J1810  197 as a function of the mass and distance to XTE J1810  197. Two independently measured distances are indicated in the figure. Minter et al. (2008) used neutral hydrogen absorption measurement to calculated a distance of 3.5  0.5 to XTE J1810  197. Durant & van Kerkwijk (2006) estimated the distance to several magnetars using red clump stars and calculated a distance of 3.1  0.5 to XTE J1810  197. We note however that there is some uncertainty in the applicability of this red clump distance estimate, since it assumes a slightly different absorption column toward XTE J1810  197 than what was used in this analysis. We can see in this plot that the only way to reconcile the tension between the distance estimates to XTE J1810  197 and a reasonable value of the NS radius is for its mass to be at least 1.9 M .

Our modeling of XTE J1810  197 utilizes simple blackbody functions rather than mag-

netized atmosphere models that may better describe the spectra of some magnetars. In the case of XTE J1810 197, however, the simple blackbody model may be most appropriate. Ruderman (1971) suggested that the strong magnetic fields near NS surfaces can lead to the formation of a condensed surface rather than an atmosphere. These condensed surfaces radiate as blackbodies, with their fluxes reduced by a factor of 0.5-0.9 compared to a blackbody with the same temperature (Potekhin 2014). It seems plausible that XTE J1810 197 could have a condensed surface, since the minimum NS radius that is a good fit to the data is about 13 km, and any atmosphere model would yield a larger radius than this blackbody model. A condensed surface model therefore makes it easier to reconcile the observational properties of XTE J1810 197 with reasonable values of neutron star radii. The critical temperature for a condensed surface on a neutron star is not well known, but it increases as a function of magnetic field strength, and the 0.15 keV surface temperature of XTE J1810 197 may be sufficiently low given the $10^{14}$ G magnetic field near the surface of XTE J1810 197.

It may not be surprising if magnetars tend to have masses larger than other neutron stars, if magnetars are born from more massive progenitors than other classes of neutron stars. There is some evidence that this may be the case: Muno et al. (2006) determined that the mass of progenitor of the magnetar CXO J164710.2 455216 likely had a mass $> 40$ M , due to its location in the massive star cluster Westerlund 1. We are of course not claiming a definitive measurement of the mass of XTE J1810 197, but the evidence is suggestive that it is more massive than the canonical 1.4 M NS. A more accurate of measurement of the distance to XTE J1810 197 would allow for a better estimate of its mass.

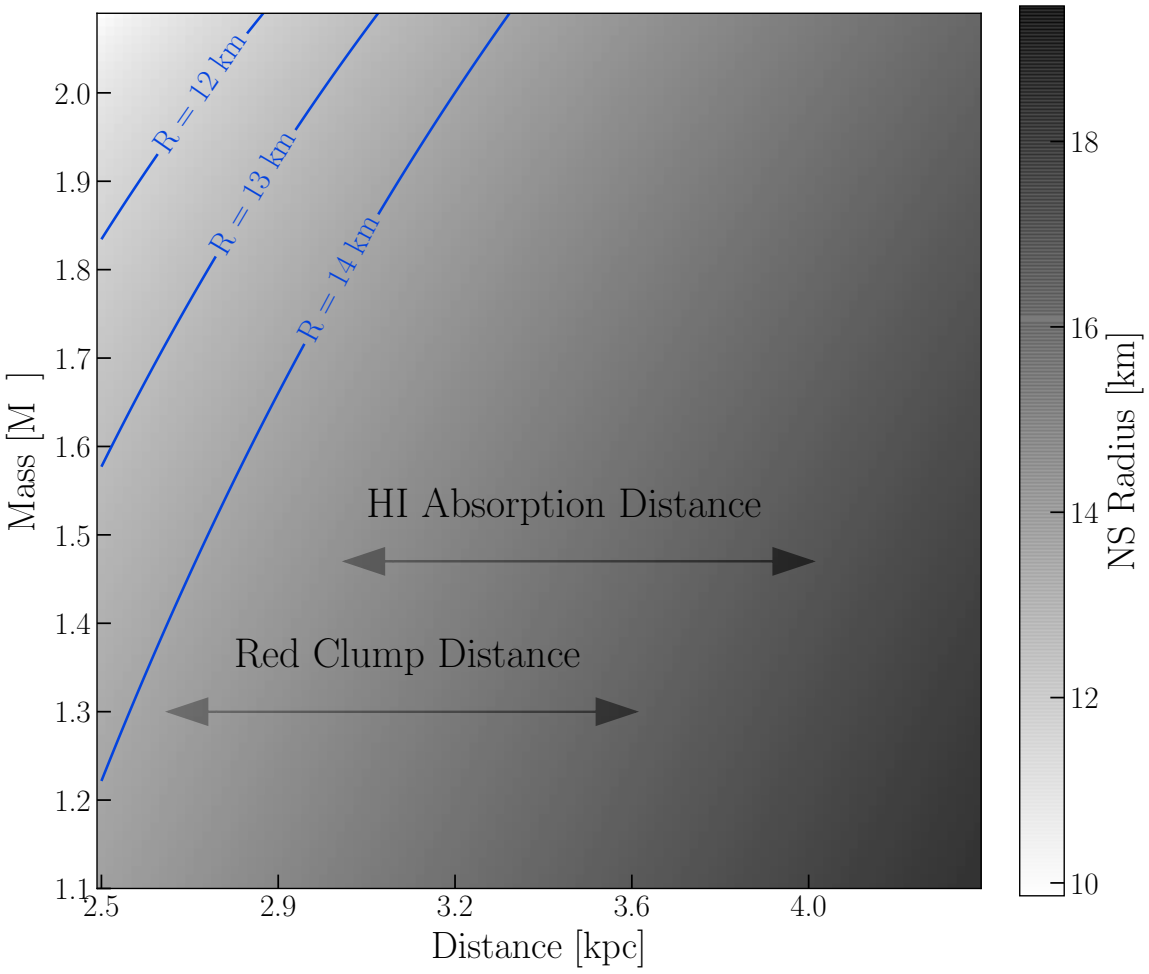


Figure 4.5: Neutron radius as a function of mass and distance. Independently measured distances are indicated by the arrows in the figure. Note that only the region in the upper left of the figure is consistent with both the independently measured distance estimates and also reasonable values of NS radii. This is evidence that XTE J1810 197 is much more massive than the canonical 1.4 M neutron star.

# Chapter 5

# Conclusion

## 5.1 Summary of Results

In this thesis I have studied surface thermal emission from a variety of young neutron stars, and drawn inferences about the physics of some of these fascinating and diverse objects. X-ray observations and modeling of central compact objects have revealed that many of them must have hot spots that cover only a small fraction of the neutron star surface. It is possible that none of them have uniform temperature carbon atmospheres that have been claimed. The non-detection of X-ray pulsations from these stars suggests that they are born with small magnetic inclination angles.

Modeling the surface thermal emission of RX J0822 4300 the central compact object in the Puppis A supernova remnant, has revealed a significant deviation from a perfectly antipodal geometry. Two hot surface regions with very different temperatures and sizes must be producing the energy dependent pulse profiles of RX J0822 4300. These measurements can now inform and constrain theories of the evolution of subsurface magnetic fields of young neutron stars.

The transient magnetar XTE J1810  197 has been shown to have soft X-ray emission from its whole surface, with a flux that when combined with distance estimates imply it is likely significantly more massive than the canonical 1.4 solar mass neutron star. We have reproduced the energy dependent pulse profiles and found that there is no evidence for anisotropic emission. XTE J1810  197 spent almost a decade in a post-outburst steady state, with a luminosity that is large enough that is must be powered from continued magnetic field decay rather than spin-down power.

## 5.2 Future Work

In late 2018, XTE J1810  197 entered into its second observed outburst. The early outburst X-ray luminosity was  5  $10^{35}$ erg s $^{1}$, and produced both pulsed X-ray and radio emission (Gotthelf et al. 2019; Dai et al. 2019). With the late 2018 X-ray outburst of XTE J1810  197 and the return of its radio emission, it may soon be possible to accurately determine the distance to XTE J1810  197 with VLBI observations. A more accurate distance estimate would allow for stronger constraints on the mass and radius of this transient magnetar. Also, continuing X-ray observations of XTE J1810  197 will give a clearer picture of the X-ray activity of this transient magnetar as it recovers from its second observed outburst.

With continuing monitoring of central compact objects, we may eventually have enough data to detect X-ray pulsations from some CCOs. Measurements of very low amplitude X-ray pulsations from some of the CCOs without known rotation periods would further confirm the picture of CCOs as young neutron stars born spinning slowly with low dipole magnetic fields. If detected, the low amplitudes would confirm that CCOs are born with small inclination angles.

Also, 1E 1207.4  5209 remains the last of the three CCOs with known rotation periods to

be modeled in detail. It has  10% pulsed fraction pulsations with equally spaced absorption features in its spectrum. The absorption features are likely due to quantum oscillations in the free-free opacity in the atmosphere (Suleimanov et al. 2010, 2012). The pulsation amplitudes are approximately constant with respect to energy, with the exception of small increases in the pulsation amplitude that correspond to the energies of its absorption features (De Luca et al. 2004). This increase in pulsed fractions at the energies of the absorption features is likely due to an anisotropic emission pattern. Successfully modeling the energy dependent pulse profiles of 1E 1207.4  5209 could give insights into the exact size and locations of its surface thermal emitting regions, as well as the details of the cyclotron absorption process in the magnetosphere.

# Bibliography

Alarie, A., Bilodeau, A., & Drissen, L. 2014, MNRAS, 441, 2996

Alford, J. A. J., & Halpern, J. P. 2016, ApJ, 818, 122

Allen, G. E., Chow, K., DeLaney, T., et al. 2015, ApJ, 798, 82

Antoniadis, J., Freire, P. C. C., Wex, N., et al. 2013, Science, 340, 448

Baade, W., & Zwicky, F. 1934, Proceedings of the National Academy of Science, 20, 259

Becker, W., Prinz, T., Winkler, P. F., & Petre, R. 2012, ApJ, 755, 141

Beloborodov, A. M. 2002, ApJ, 566, L85

—. 2009, ApJ, 703, 1044

Bernardini, F., Perna, R., Gotthelf, E. V., et al. 2011, MNRAS, 418, 638

Bernardini, F., Israel, G. L., Dall'Osso, S., et al. 2009, A&A, 498, 195

Bogdanov, S. 2014, ApJ, 790, 94

Buccheri, R., Bennett, K., Bignami, G. F., et al. 1983, A&A, 128, 245

Camilo, F., Ransom, S. M., Halpern, J. P., & Reynolds, J. 2007, ApJ, 666, L93

Camilo, F., Ransom, S. M., Halpern, J. P., et al. 2006, Nature, 442, 892

—. 2016, ApJ, 820, 110

Cassam-Chenaï, G., Decourchelle, A., Ballet, J., et al. 2004, A&A, 427, 199

Chang, P., & Bildsten, L. 2003, ApJ, 585, 464

Cromartie, H., Fonseca, E., Ransom, S. M., et al. 2019, arXiv e-prints, arXiv:1904.06759

Cumming, A., Arras, P., & Zweibel, E. 2004, ApJ, 609, 999

Dai, S., Lower, M. E., Bailes, M., et al. 2019, ApJ, 874, L14

Dall'Osso, S., & Perna, R. 2017, MNRAS, 472, 2142

De Luca, A. 2017, in Journal of Physics Conference Series, Vol. 932, Journal of Physics Conference Series, 012006

De Luca, A., Mereghetti, S., Caraveo, P. A., et al. 2004, A&A, 418, 625

Demorest, P. B., Pennucci, T., Ransom, S. M., Roberts, M. S. E., & Hessels, J. W. T. 2010, Nature, 467, 1081

Doroshenko, V., Suleimanov, V., & Santangelo, A. 2018, A&A, 618, A76

Duncan, R. C., & Thompson, C. 1992, ApJ, 392, L9

Durant, M., & van Kerkwijk, M. H. 2006, ApJ, 650, 1070

Esposito, P., Rea, N., Borghese, A., et al. 2020, arXiv e-prints, arXiv:2004.04083

Fahlman, G. G., & Gregory, P. C. 1981, Nature, 293, 202

Gaensler, B. M., Tanna, A., Slane, P. O., et al. 2008, ApJ, 680, L37

Geppert, U., Küker, M., & Page, D. 2004, A&A, 426, 267

—. 2006, A&A, 457, 937

Geppert, U., Page, D., & Zannias, T. 1999, A&A, 345, 847

Geppert, U., & Viganò, D. 2014, MNRAS, 444, 3198

Giacani, E., Smith, M. J. S., Dubner, G., et al. 2009, A&A, 507, 841

Giacani, E. B., Dubner, G. M., Green, A. J., Goss, W. M., & Gaensler, B. M. 2000, AJ, 119, 281

Glampedakis, K., Jones, D. I., & Samuelsson, L. 2011, MNRAS, 413, 2021

Gold, T. 1968, Nature, 218, 731

Goldreich, P., & Reisenegger, A. 1992, ApJ, 395, 250

Gonzalez, D., & Reisenegger, A. 2010, A&A, 522, A16

Gotthelf, E. V., & Halpern, J. P. 2007, Ap&SS, 308, 79

—. 2009, ApJ, 695, L35

Gotthelf, E. V., Halpern, J. P., & Alford, J. 2013, ApJ, 765, 58

Gotthelf, E. V., Halpern, J. P., & Seward, F. D. 2005, ApJ, 627, 390

Gotthelf, E. V., Perna, R., & Halpern, J. P. 2010, ApJ, 724, 1316

Gotthelf, E. V., Halpern, J. P., Alford, J. A. J., et al. 2019, ApJ, 874, L25

Gourgouliatos, K. N., & Hollerbach, R. 2018, ApJ, 852, 21

Greenstein, G., & Hartke, G. J. 1983, ApJ, 271, 283

Gregory, P. C., & Fahlman, G. G. 1980, Nature, 287, 805

Groth, E. J. 1975, ApJS, 29, 285

Halpern, J. P., & Gotthelf, E. V. 2010, ApJ, 709, 436

Halpern, J. P., Gotthelf, E. V., Becker, R. H., Helfand , D. J., & White, R. L. 2005, ApJ, 632, L29

Hewish, A., Bell, S. J., Pilkington, J. D. H., Scott, P. F., & Collins, R. A. 1968, Nature, 217, 709

Heyl, J. S., & Hernquist, L. 1998, MNRAS, 300, 599

Ho, W. C. G. 2011, MNRAS, 414, 2567

Ho, W. C. G., & Heinke, C. O. 2009, Nature, 462, 71

Ho, W. C. G., Potekhin, A. Y., & Chabrier, G. 2008, ApJS, 178, 102

Hollerbach, R., & Rüdiger, G. 2002, MNRAS, 337, 216

Ibrahim, A. I., Markwardt, C. B., Swank, J. H., et al. 2004, ApJ, 609, L21

Klochkov, D., Pühlhofer, G., Suleimanov, V., et al. 2013, A&A, 556, A41

Klochkov, D., Suleimanov, V., Sasaki, M., & Santangelo, A. 2016, A&A, 592, L12

Kouveliotou, C., Dieters, S., Strohmayer, T., et al. 1998, Nature, 393, 235

Lai, D. 2001, Reviews of Modern Physics, 73, 629

Landau, L. D. 1932, Phys. Zs. Sowjet, 1, 285

Levin, L., Bailes, M., Bates, S., et al. 2010, ApJ, 721, L33

Linares, M., Shahbaz, T., & Casares, J. 2018, ApJ, 859, 54

Margalit, B., & Metzger, B. D. 2017, ApJ, 850, L19

Mazets, E. P., Golentskii, S. V., Ilinskii, V. N., Aptekar, R. L., & Guryan, I. A. 1979, Nature, 282, 587

McClure-Griffiths, N. M., Green, A. J., Dickey, J. M., et al. 2001, ApJ, 551, 394

Michel, F. C., & Goldwire, H. C., J. 1970, Astrophys. Lett., 5, 21

Minter, A. H., Camilo, F., Ransom, S. M., Halpern, J. P., & Zimmerman, N. 2008, ApJ, 676, 1189

Mori, K., & Ho, W. C. G. 2007, MNRAS, 377, 905

Muno, M. P., Clark, J. S., Crowther, P. A., et al. 2006, ApJ, 636, L41

Oppenheimer, J. R., & Volkoff, G. M. 1939, Physical Review, 55, 374

Page, D. 1995, ApJ, 442, 273

Pavlov, G. G., Zavlin, V. E., Aschenbach, B., Trümper, J., & Sanwal, D. 2000, ApJ, 531, L53

Pavlov, G. G., Zavlin, V. E., & Trümper, J. 1999, ApJ, 511, L45

Pechenick, K. R., Ftaclas, C., & Cohen, J. M. 1983, ApJ, 274, 846

Pérez-Azorín, J. F., Miralles, J. A., & Pons, J. A. 2006, A&A, 451, 1009

Perna, R., & Gotthelf, E. V. 2008, ApJ, 681, 522

Perna, R., & Pons, J. A. 2011, ApJ, 727, L51

Perna, R., Viganò, D., Pons, J. A., & Rea, N. 2013, MNRAS, 434, 2362

Petre, R., Becker, C. M., & Winkler, P. F. 1996, ApJ, 465, L43

Petre, R., Kriss, G. A., Winkler, P. F., & Canizares, C. R. 1982, ApJ, 258, 22

Philippov, A., Tchekhovskoy, A., & Li, J. G. 2014, MNRAS, 441, 1879

Pons, J. A., Miralles, J. A., & Geppert, U. 2009, A&A, 496, 207

Pons, J. A., & Perna, R. 2011, ApJ, 741, 123

Potekhin, A. Y. 2014, Physics Uspekhi, 57, 735

Potekhin, A. Y., & Yakovlev, D. G. 2001, A&A, 374, 213

Reynolds, S. P., Borkowski, K. J., Hwang, U., et al. 2006, ApJ, 652, L45

Reynoso, E. M., Cichowolski, S., & Walsh, A. J. 2017, MNRAS, 464, 3029

Rookyard, S. C., Weltevrede, P., & Johnston, S. 2015a, MNRAS, 446, 3367

—. 2015b, MNRAS, 446, 3356

Ruderman, M. 1971, Phys. Rev. Lett., 27, 1306

Sánchez-Ayaso, E., Combi, J. A., Albacete Colombo, J. F., et al. 2012, Ap&SS, 337, 573

Shabaltas, N., & Lai, D. 2012, ApJ, 748, 148

Shannon, R. M., & Johnston, S. 2013, MNRAS, 435, L29

Suleimanov, V. F., Klochkov, D., Pavlov, G. G., & Werner, K. 2014, ApJS, 210, 13

Suleimanov, V. F., Klochkov, D., Poutanen, J., & Werner, K. 2017, A&A, 600, A43

Suleimanov, V. F., Pavlov, G. G., & Werner, K. 2010, ApJ, 714, 630

—. 2012, ApJ, 751, 15

Suleimanov, V. F., Poutanen, J., Klochkov, D., & Werner, K. 2016, European Physical Journal A, 52, 20

Tauris, T. M., & Manchester, R. N. 1998, MNRAS, 298, 625

Thompson, C., & Duncan, R. C. 1996, ApJ, 473, 322

Tian, W. W., Leahy, D. A., Haverkorn, M., & Jiang, B. 2008, ApJ, 679, L85

Viganò, D., & Pons, J. A. 2012, MNRAS, 425, 2487

Viganò, D., Rea, N., Pons, J. A., et al. 2013, MNRAS, 434, 123

Yakovlev, D. G., Haensel, P., Baym, G., & Pethick, C. 2013, Physics Uspekhi, 56, 289

Yan, T., Perna, R., & Soria, R. 2012, MNRAS, 423, 2451

Zane, S., & Turolla, R. 2006, MNRAS, 366, 727

Zavlin, V. E., Pavlov, G. G., Sanwal, D., & Trümper, J. 2000, ApJ, 540, L25